Journal of
Nuclear Engineering

MDPI

Article

Engineering the Next Generation of Industrially Scalable Fusion-Grade Steels

David Bowden [1,*], Benjamin Evans [1], Jack Haley [1], Jim Johnson [1], Alexander Carruthers [1], Stephen Jones [2], Dane Hardwicke [2], Talal Abdullah [2], Shahin Mehraban [2], Nicholas Lavery [2], Paul Sukpe [3], Richard Birley [4], Abdollah Bahador [4], Alan Scholes [4] and Peter Barnard [1,4]

[1] United Kingdom Atomic Energy Authority, Culham Campus, Culham OX14 3DB, UK; ben.evans@ukaea.uk (B.E.); jim.johnson@ukaea.uk (J.J.)
[2] Faculty of Science and Engineering, Swansea University, Bay Campus, Fabian Way, Swansea SA1 8EN, UK; stephen.p.jones@swansea.ac.uk (S.J.); d.w.hardwicke@swansea.ac.uk (D.H.); s.mehraban@swansea.ac.uk (S.M.)
[3] Department of Mechanical Engineering, Imperial College London, South Kensington Campus, London SW7 2AZ, UK; p.sukpe@imperial.ac.uk
[4] Materials Processing Institute, Eston Road, Middlesbrough TS6 6US, UK; abdollah.bahador@mpiuk.com (A.B.)
* Correspondence: david.bowden@ukaea.uk

Abstract

Future fusion power plants require structural materials that can withstand extreme operating conditions, including high coolant outlet temperatures, mechanical loading, and radiation damage. Reduced-activation ferritic martensitic (RAFM) steels are a primary candidate as a structural material for such applications. This study demonstrates the successful production of a 5.5-tonne RAFM billet via electric arc furnace (EAF) technology, enabling scalable, cost-effective manufacturing. The resulting UK-RAFM alloy offers superior tensile strength and creep lifetime performance compared to Eurofer97. This is attributed to alterations in the initial forging process during manufacture. Modified thermomechanical treatments (TMTs) were subsequently applied to the UK-RAFM, which are shown to enhance the tensile strength further, particularly at 650 °C. Building on this, an Advanced RAFM (ARAFM) steel was designed to exploit the benefits of optimised chemistry to encourage metal carbonitride (MX) precipitate evolution alongside bespoke TMTs. Challenges around ensuring suitable processing windows in these steels, to avoid the over-coarsening of MX precipitates or the formation of deleterious delta-ferrite, are discussed. A subsequent 5.5-tonne ARAFM billet has since been produced using EAF facilities, with performance to be reported separately. This work highlights the synergy between alloy design, process optimisation, and industrial scalability, paving the way for a new generation of low-cost, high-volume, fusion-grade steels.

Keywords: fusion; steel; creep; tensile; toughness; industrialisation; processing

Academic Editor: Dan Gabriel Cacuci

Received: 27 October 2025
Revised: 4 December 2025
Accepted: 10 December 2025
Published: 19 December 2025

1. Introduction

Proposed commercial fusion powerplant concepts plan to utilise structural materials with tailored compositions to limit the level of radioactivity after shutdown. Steels such as European Eurofer97, Japanese F82H, Indian INRAFM, Korean ARAA and Chinese CLAM are examples of reduced-activation ferritic martensitic (RAFM) steel [1–5]. These alloys are designed to minimise elements such as nickel, niobium and molybdenum within the alloy

composition, in favour of reduced radioactivation elements such as tungsten, tantalum and vanadium. These steels are utilised primarily within the breeder blanket components and must endure a range of challenging operational requirements, including high levels of radiation damage, long-term and cyclic mechanical loads and high temperatures, to name just a few. Commercial fusion machines will require enhanced thermal efficiencies to deliver sufficient levels of net energy output for economic viability. As such, coolant outlet temperatures up to 650 °C may be required for machines such as the Spherical Tokamak for Energy Production (STEP Fusion) [6,7]. Increasing the separation between the inlet and outlet coolant temperatures will maximise the plant efficiency according to the Carnot cycle.

However, conventional RAFM steels suffer from poor creep lifetimes during operation above 550 °C, summarised in Figure 1. In recent decades, efforts to increase the high temperature creep resistance of RAFM steels have focussed on increasing the density of stable metal carbonitride (MX) nano-precipitates [8–15]. The high density of stable precipitates performs two primary functions: contributing toward strengthening but also significantly increasing the sink strength of irradiation-induced defects, thereby greatly increasing neutron damage resistance. The MX particles can also act as effective trapping sites for neutron-induced helium in the lattice. This helps prevent the creation of large cavities and weakened grain boundaries during operation in reactor environments. Both mechanisms reduce embrittlement during service and the associated risk of premature failure [16,17]. Developed by Oak Ridge National Laboratory (ORNL), the Castable Nanostructured Alloys (CNAs), reported in Figure 1, utilise TiC MX strengthening, achieving high precipitate densities [18]. Whilst exceeding the creep performance of conventional Eurofer97 at 650 °C, the CNAs failed to outperform Eurofer97 when utilising normalisation temperatures of 1150 °C and tempering at 700 °C [19]. As an alternative route, EUROfusion successfully demonstrated substantially enhanced creep strengthening through a series of high W (up to 3 wt.%) and boron-additive steels [20].

Thermo-mechanical treatments (TMTs) are the chosen method to produce the high density of nano-precipitates. TMTs involve deformation in the austenite regime, encouraging deformation induced dislocations, at which precipitates preferentially nucleate. Klueh et al. introduced N containing steels processed with TMTs to increase precipitation of MX nano-precipitates, which are a combination of V and Ta-rich carbides and nitrides [15,21,22]. They were able to develop steels with a much higher number density and much smaller size of precipitates than conventionally treated steels. A similar approach was applied as early as 1998 by Hasegawa et al. [23]. Nitride strengthening can also greatly increase the high temperature properties of RAFM steels, as shown by a number of authors who have followed this trend in recent years [14,24–27]. These authors produced Eurofer97-type steels with levels of N ranging from 0.01 to 0.076 wt.% N, with most around 0.05 wt.% N. Klueh states that these levels of N should not compromise the reduced activation properties of the steels [28]. However, specific limits on nitrogen in reduced activation materials varies depending on country-specific legislation on radioactive waste classification. The UK limit on ^{14}C generation (produced from the transmutation of ^{14}N) is more constrained compared to other countries, such as France where activity is accounted for on a 'per-isotope' basis [29].

Numerous attempts have been made to improve the properties of Eurofer97-type steels using various heat treatments and TMTs [30,31]. Rieth et al. compared ten different neutron irradiated Eurofer97-type steels, each with varying compositions and TMTs. A steel produced by Puype et al. [27] ("Alloy J") is the current state of the art in terms of irradiation resistance, with similar levels of irradiation-induced degradation of mechanical properties compared to other grades, but with improved post-irradiation fracture toughness

properties. This review concluded that the effect of heat treatments on final irradiated properties outweighs that of composition [31].

The TMT used by Puype et al. had several stages [27]. The material was initially heated to 1250 °C for 1 h before being hot-rolled. The rolled material was then air cooled to room temperature, before being annealed. Four different annealing temperatures were investigated, namely 880, 920, 980 and 1050 °C, followed by water quenching. The final stage was a temper at 750 °C for 2 h followed by air cooling. The initial normalisation at 1250 °C converts all ferrite to austenite and dissolves all existing precipitates. Hot rolling introduces a high density of dislocations that act as nucleation sites for a fine distribution of MX precipitates which form during the annealing stage. The annealed microstructures all show relatively equiaxed grains with a clear increase in grain size with increasing annealing temperature. Other authors have also used an intermediate annealing step between rolling and tempering for control of precipitates, the main motivation being the suppression of $M_{23}C_6$ precipitation to favour MX precipitation [32–35].

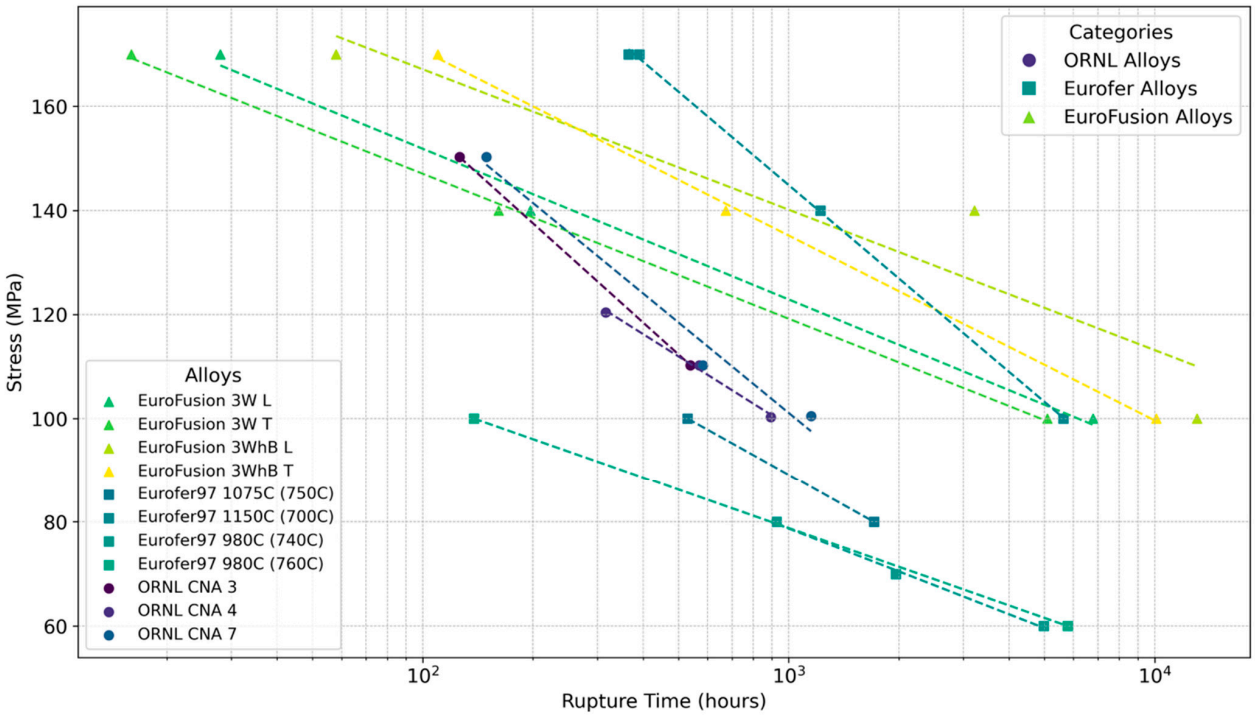

Figure 1. Creep lifetimes for Eurofer97, EUROfusion high W variants and CNAs. Data reported for creep tests at 650 °C. Data from: [18–20,36].

2. The UK Alloy Design Strategy

In the UK, efforts led through a national consortium, with linkages to international irradiation capabilities, are focussed on building upon existing high-temperature steel research, to generate nano-strengthened Advanced RAFM (ARAFM) steels and boron-strengthened RAFM (BRAFM) variants [37]. These two classes of steel build upon the knowledge developed around high temperature steels, particularly the use of MX carbide/nitride strengthening and thermo-mechanical treatments (TMTs). Internationally, these steels are typically produced using vacuum induction melting (VIM) plus electro-slag remelting (ESR) or vacuum arc remelting (VAR) [36,38,39]. In contrast, the UK approach has been towards ensuring industrial scalability utilising nationally available and high-volume electric arc furnace (EAF) facilities, reliant on a high-quality and well-understood scrap supply chain. This approach offers a significant cost reduction and a substantial increase in

steel production volume compared to VIM + ESR/VAR. The programme spearheading this development consortium is named NEUtron iRradiatiOn of advaNced stEels (NEURONE).

NEURONE is a GBP ~15m programme with the aim to develop and deliver an industrially scalable fusion-grade ARAFM and BRAFM steel capable of operating in a fusion breeder-blanket environment. In this context, 'fusion-grade' steels possess several properties which enhance their favourability to operate in a fusion environment. By removing high-activity elements such as Ni, Co and Nb from their specification, these steels are generally expected by the wider fusion community to meet low-level waste classification within 100 years of decommissioning [37,40,41]. These steels also reduce elements which may lead to subsequent degradation of the alloy during normal operation, such as Si, P, S and O. Such degradation may occur as a result of radiation damage [42–44], or subsequent machining operations through welding and joining (such as P and S degrading welded regions [45]). In addition, 'fusion-grade' alloys are specifically designed to tolerate the challenging conditions in which they must operate within a fusion plant, this may necessitate reduced irradiation-induced swelling, elevated temperature strength, creep resistance, and sufficient toughness.

The NEURONE programme commenced in 2024 and will complete in 2028. Eleven organisations are involved in the core programme, across academia, research technology organisations (RTO), and industry. A two-step approach is being utilised to develop NEURONE alloys. Firstly, the alloy chemistry is being modified to exploit the strengthening effects imparted through precipitate strengthening, as well as control of elements susceptible to deleterious effects under irradiation. Secondly, TMTs are being devised to exploit the formation of MX precipitates in these steels using carefully sequenced rolling and heat treatment cycles.

NEURONE is approaching steel design considerations from two crucial perspectives. Firstly, high temperature strength is to be enhanced, enabling the potential for steel operation up to a stretch goal of 650 °C. This is achieved through a combination of chemistry and TMT control, encouraging the formation of MX precipitates. These precipitates act to pin dislocations, prevent grain boundary sliding and act as sinks for radiation damage. Secondly, low temperature toughness is to be enhanced, with a particular view to delay the onset of low-temperature hardening embrittlement (LTHE) during irradiation, which typically occurs below 350 °C. Refined prior austenite grain (PAG) size was suggested by Bhattacharya et al. to be a critical strategy in delaying the LTHE of neutron irradiated RAFM steels [46]. The PAG size is primarily controlled via the TMT process parameters. However, a refined grain size comes at the expense of creep performance. Therefore, NEURONE will explore the effect of gradual coarsening of grain sizes to strike an optimal balance between creep and toughness properties. Therefore, the ultimate goal of NEURONE is to produce a hybridised steel capable of performing across a sufficiently broad operational window to allow use across a breeder blanket component, where peak temperatures could reach 650 °C, and enhanced toughness will be required in cooler regions close to the LTHE onset temperature at ~350 °C.

When considering the chemistry of NEURONE alloys; vanadium nitride (VN) and tantalum carbide (TaC) precipitation have been explored in the initial round of alloy development. These MX precipitates will be crucial to enhance high-temperature creep performance, as well as the irradiation damage tolerance of the alloy. Initial studies focussed on the radiation tolerance of early NEURONE alloys, observed dissolution of VN above a dose of 40 displacements per atom (dpa) during self-ion (Fe) irradiation [47]. This may indicate an inherent limitation for VN to tolerate high levels of damage. Future studies intend to address whether this effect arose as a result of a high dose rate or the distinct needle-like morphology of the observed VN. Mn and Si levels are also being

suppressed to levels as low as 0.05 wt.% to control the well-documented clustering effects that these elements are susceptible to during irradiation [42–44]. W is utilised as a solid solution strengthener, and its levels are enhanced up to 2 wt.% to enhance the alloy's high-temperature strength. Cr levels of 8–9 wt.% have been utilised, high enough to enable sufficient corrosion resistance in aqueous environments, low enough to ensure austenite (γ) stability, and within the suggested minima level to reduce the irradiation-induced ductile to brittle transition temperature (DBTT) shift [48].

One primary objective within NEURONE is to demonstrate scalability using industrially relevant processes, namely using electric arc furnace (EAF) facilities. Future fusion machines, such as the STEP Fusion machine may require in the region of 1000 to 5000 tonnes of structural steel. Clearly, industrial scale up at a competitive price-point will be required to meet this demand, particularly when considering requirements for a future fleet of commercial machines. Conventional RAFM routes have focussed on VIM + ESR/VAR [36,38,39]. These routes are more intensive than EAF alone and yields are constrained compared to EAF. Production via the EAF route is anticipated to present an order of magnitude cost reduction compared to VIM + ESR/VAR. One of the main challenges associated with EAF production is sourcing suitable feedstock materials, usually from scrap sources, which offer the required cleanliness to meet the stringent activation targets for RAFM steels. In addition, caution will be required to ensure that oxygen and other gaseous contents are minimised during EAF processing, which unlike VIM, does not benefit from minimisation/removal of gases during the melt. Therefore, oxidation losses and reaction with the slag can make compositional control more challenging when using the EAF route, compared to VIM. Additional steps such as vacuum arc degassing (VAD), ESR and VAR offer additional options to improve EAF billet compositional quality if required, however.

At the other end of the spectrum, oxide dispersion strengthened (ODS) steels are a competitor alloy class to the ARAFMs and other enhanced RAFM variants being developed, but are limited to powder metallurgy process routes, requiring intensive atomisation, ball-milling and consolidation steps to reach the final product [49]. This severely constrains yields and increases the cost substantially. These factors are shown schematically in Figure 2.

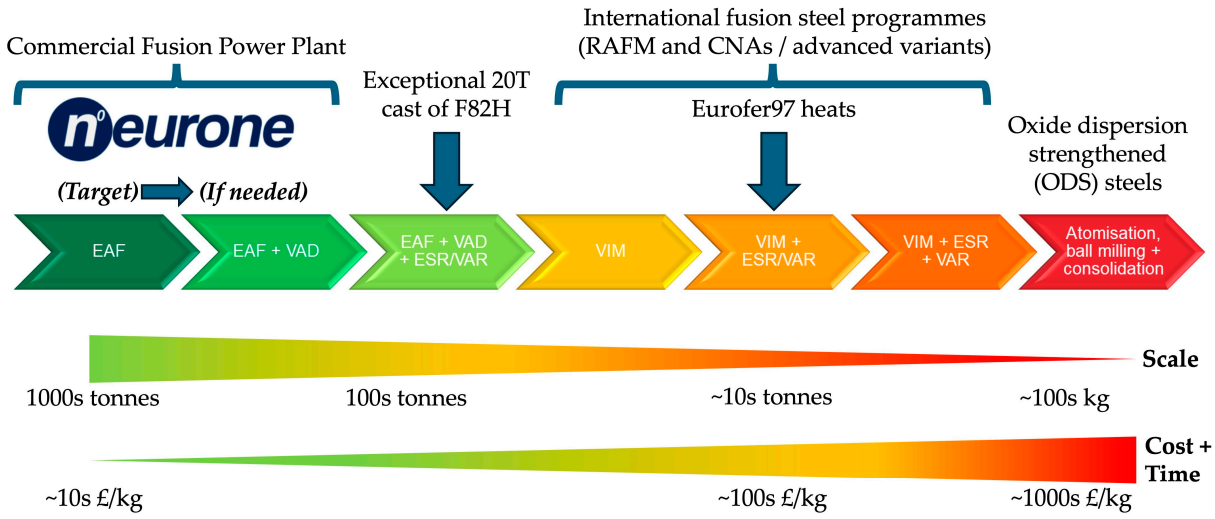

Figure 2. Schematic representation of the various steel processing routes considered in the field, and comparative values of both cost and scale. NEURONE is shown targeting an EAF-only approach, with secondary VAD or other steps considered only if needed for improved cleanliness. Eurofer97 heats are outlined in [50], whilst the exceptional 20T F82H cast is outlined in [51].

Whilst NEURONE is a broad programme, this paper explores three key facets being explored. Firstly, the scalability of a Eurofer97-like RAFM alloy using the EAF will

be discussed, and the microstructure and mechanical performance of this alloy (named UK-RAFM) will be compared to conventional VIM+ESR/VAR counterparts. Secondly, the application of a modified TMT to the UK-RAFM alloy and the resultant impact on alloy performance will be examined (named Modified UK-RAFM). Finally, the development of specific subset of laboratory-scale (Lab-scale) ARAFM steel will be explored in more detail, outlining the chemical and process parameter effects on the resultant material microstructure and performance. The reader is advised that for clarity and ease of comparison, the results for the three alloys may appear side by side in figures, whilst the relevant alloys will be introduced in latter parts of the paper.

3. Application of Electric Arc Furnace Production for Fusion Steels

3.1. Electric Arc Furnace Production Process

For the initial EAF production trial, an alloy targeting a composition identical to Eurofer97 was produced. As this alloy is not officially Eurofer97, and as is explained below, has several distinct differences, it has been named UK-RAFM. The UK-RAFM billet was produced by the Materials Processing Institute (MPI), Middlesbrough UK at the Normanton Plant. A 7-tonne EAF was used to deliver a 5.5-tonne billet of UK-RAFM, which was continuously cast into the dimensions of 0.3 m × 0.14 m × 13 m. The feedstock materials used were melting-based iron (from blast-furnace facilities), which were analysed in-house to verify compositional quality. The alloying elements were added in the form of either pure elements (99.99% purity) or master alloys. While Cr and Ta were added as pure elements, V, W, and Mn were added in the form of FeV, FeW, and FeMn master alloys. Notably, analytical grade source materials were not used, in order to more accurately represent a viable commercial supply chain for these materials in the future. Figure 3a,b show the resultant billet, passing through the product straightener after continuous casting, and cooling on the shop floor, respectively.

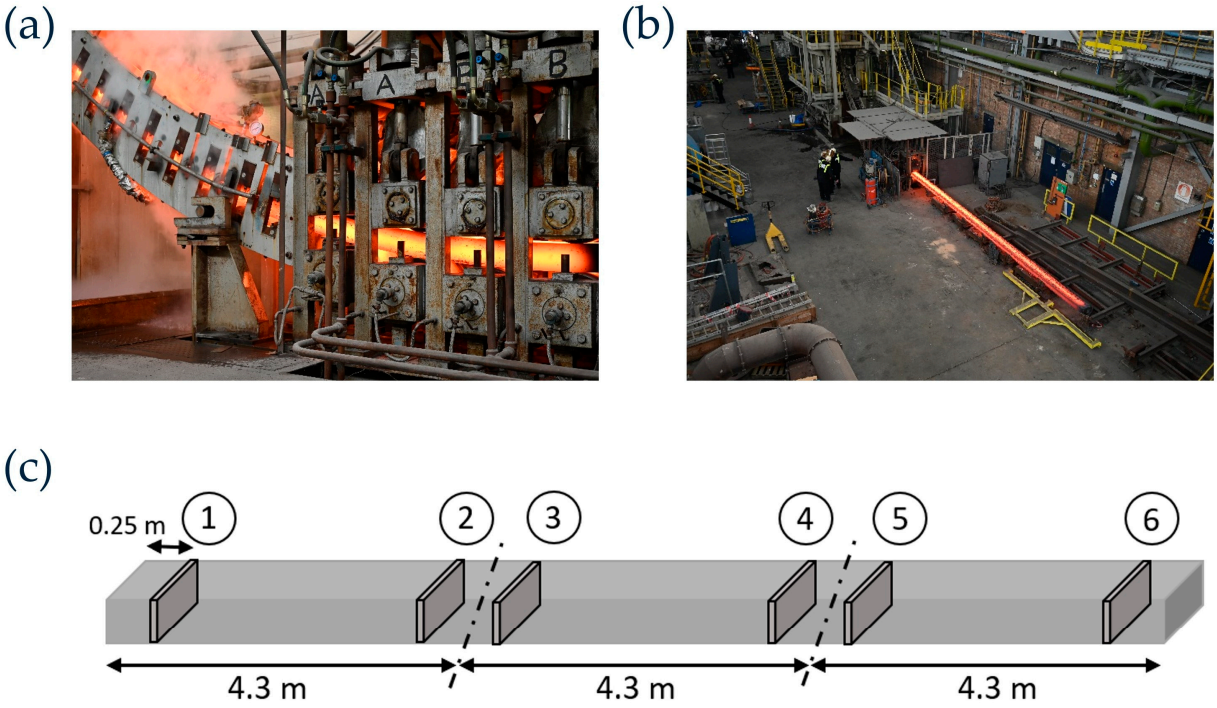

Figure 3. (**a**) Photograph of the UK-RAFM EAF billet passing from the continuous caster and entering the straightener. (**b**) The UK-RAFM billet on the shop floor at MPI. (**c**) Schematic of UK-RAFM billet and locations used to extract initial sections for processing. The circled numbers indicate locations where plate sections were extracted.

Subsequently, sections of 35 mm-thickness were removed from the billet as shown in Figure 3c. These were sectioned along the centreline and rolled into two plates (either 10 or 14 mm thickness). These were processed according to the following schedule: Solution treatment at 1200 °C for 150 min, forging down to 24 mm for the 14 mm plate and 22 mm for the 10 mm plate. The forged sections were reheated and rolled at 1200 °C to the final thicknesses of either 14 mm (~60% total reduction) or 10 mm (~70% total reduction) in three passes. This was followed by normalisation at 980 °C for 38 min with air cooling, in accordance with the typical process schedule for Eurofer97 [36]. Finally, the plates were tempered at 760 °C for 90 min, followed by air cooling. The 14 mm-thick plates are discussed in this study, whilst the 10 mm-thick plates are being utilised for welding studies and will be reported on separately.

Whilst the heat treatment replicates what is reported for Eurofer97, the forging steps are however not publicly available, hence these likely deviate from the typical Eurofer97 specification.

3.2. UK-RAFM Characterisation

Subsequently, rolled and heat-treated UK-RAFM plates were analysed using SpectroLab (Kleve, Germany) optical emission spectroscopy (OES) analyser within the MPI characterisation laboratories, to confirm the chemical composition of the ingot. Additional combustion analysis was performed at Swansea University, utilising a LECO CS744 analyser (St. Joseph, MI, USA) for precise quantification of carbon (C) and sulphur (S) contents, and an ELTRA ON-900 instrument (Haan, Germany) for oxygen (O) and nitrogen (N) determinations.

The reported composition of the UK-RAFM ingot is shown in Table 1. Notably, the Cr, Ni, and Si contents are outside of the specified Eurofer97 limits. It is believed that the Ni was present in the melting-based iron, and future melts will seek to minimise these residuals in the feedstock material.

Table 1. Alloy compositions shown in wt.%. ALAP = as low as possible.

Alloy Name	Cr	Ni	W	Ta	V	Mn	Mo	Nb	Si	C	N	P	S	Co	Cu	O	Fe
Eurofer97 [1]																	
Min/	8.5	ALAP	1.0	0.10	0.15	0.20	ALAP	ALAP	ALAP	0.09	0.015	ALAP	ALAP	ALAP	ALAP	ALAP	Bal.
Max/	9.5	0.01	1.2	0.14	0.25	0.60	0.005	0.005	0.05	0.12	0.045	0.005	0.005	0.01	0.01	0.01	
Target	9.0	ALAP	1.1	0.12		0.40				0.11	0.030						
UK-RAFM actual	10.115	0.020	1.004	0.092	0.223	0.457	<0.0005	<0.0005	0.147	0.11	0.023	0.009	0.004	0.010	0.010	0.007	Bal.
Lab-scale ARAFM																	
Target/	9.0	ALAP	2.0	ALAP	0.3	0.4	ALAP	ALAP	ALAP	0.07	0.03	ALAP	ALAP	ALAP	ALAP	ALAP	Bal.
Actual	8.89	0.030	2.1	<0.01	0.33	0.38	<0.003	<0.001	0.2	0.06	0.035	0.005	<0.003	<0.01	<0.01	0.083	

Noting the deviation from the specified compositional limits, activation analysis was conducted using FISPACT-II and the database derived from calculated activities arising from the DEMO neutron spectrum observed at the outboard first wall for 2 full power years [52]. Elemental activities were summed according to compositional weighting to produce an approximation of β+γ activity and γ contact-dose rate for UK-RAFM, Lab-scale ARAFM, Eurofer97 Batch EF3i [53], Grade 92 [54] and ITER Grade 316LN(-IG) [55]. These findings are shown in Figure 4. The complete compositions used for the FISPACT-II analysis, including impurity elements, are shown in Supplementary Table S1. Notably, neither UK-RAFM or Eurofer97 satisfies the UK β+γ low-level waste (LLW) criteria after 100 years post-operation (Figure 4a), and such results have been observed elsewhere in the literature for steels [40]. After 100 years of decay, UK-RAFM has an activity of 183 MBq/kg compared to 148 MBq/kg in Eurofer97 EF3i. This increase in UK-RAFM activity is primarily

driven by a slightly higher level of Cu (0.01 wt.% vs. 0.003 wt.%), although the UK-RAFM Cu content does remain within the Eurofer97 specification. This is a potential cause for concern due to the reliance on scrap feedstock for future EAF melts, and the accumulating levels of Cu present in recycled steels. Other notable elements, in order of significance are N (whereby UK-RAFM achieves a lower result, within the Eurofer97 specification), Ni (which is out of specification by double the amount in the UK-RAFM) and Zn (which was not reported for Eurofer97 EFi3, nor specified in the Eurofer97 target composition). This compares to 2432 MBq/kg for Grade 92 steel, and 30302 MBq/kg for 316LN-IG, neither of which are reduced activation steels.

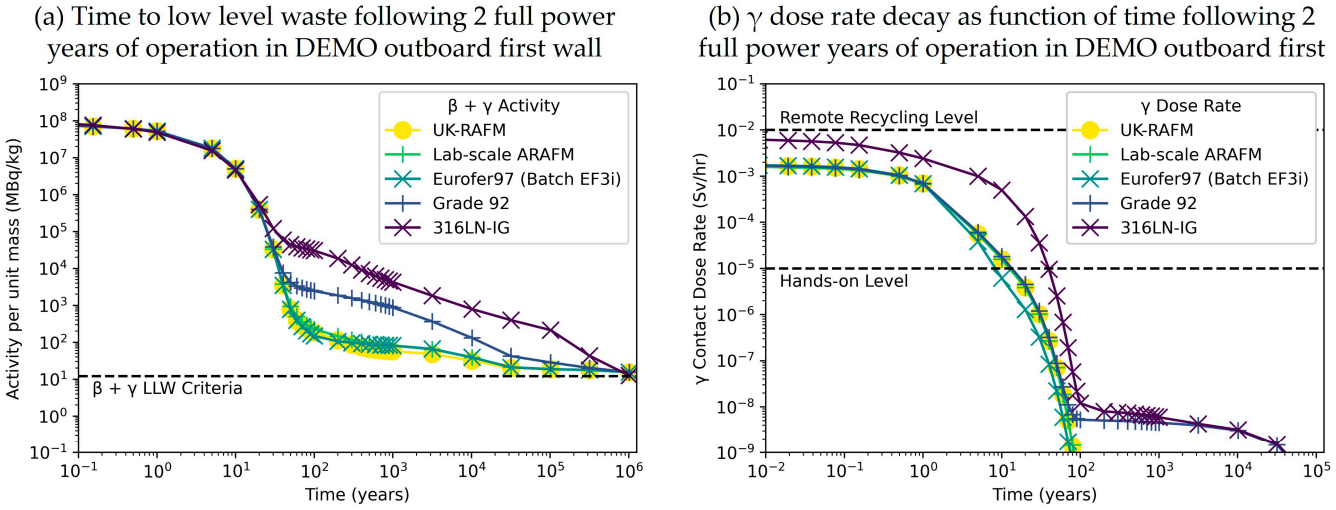

Figure 4. FISPACT-II activation analysis for UK-RAFM and Lab-scale ARAFM steel compared to Eurofer97 [1], Grade 92 [54], and 316LN-IG [55]. Results calculated for (**a**) time to reach the UK β+γ LLW criteria and (**b**) γ contact dose rate as a function of time, in both cases following 2 full power years in the DEMO outboard first wall.

A more achievable target for reduced activation steels would be reaching human handleability (limited by γ dose rate, rather than β+γ activity) for processing within a much shorter timeframe, allowing for the recycling of high-value steel components rather than disposal [56,57]. From a maintenance perspective, Eurofer97 offers a shorter time (~10 years) to achieve a maximum contact dose of 0.01 $mSv \cdot hr^{-1}$ for hands-on processing [58], in comparison to the UK-RAFM, which reaches this level after ~15 years (Figure 4b). Co content is a key driver to achieving an acceptable contact dose level. The difference in time between Eurofer97 and UK-RAFM is due to the increased Co content (although UK-RAFM is still within the Eurofer97 specification). As Co content is not explicitly stated for Grade 92 and 316LN-IG, an assumed Co impurity arising from the Ni content (2% impurity fraction, derived from [59]) was used in these calculations (values shown in Supplementary Table S1). As a validation step, it was determined that this assumption was a reasonable representation of the measured Co content in low-Ni, RAFM steels discussed in this paper. For comparison purposes, Grade 92 steel requires ~16 years, and 316LN-IG requires ~40 years to reach acceptable γ contact dose limits. In all cases here, the FISPACT-II analysis indicates that some relaxation on certain compositional limits may be acceptable whilst still achieving a reduced-activation specification. This would further alleviate significant challenges for steel manufacturers when seeking to produce RAFM steels at tonnage scales for a commercial plant.

Small ~1 cm^3 samples were removed from the UK-RAFM 14 mm-thick plate for microstructural analysis. Samples were prepared for scanning electron microscopy (SEM) through standard metallographic polishing techniques, using SiC papers and diamond

suspension down to 1 µm, and finished with colloidal silica. Electron backscatter diffraction (EBSD) was carried out using a Tescan Mira3 microscope (Brno, Czech Republic) and Oxford Instruments Symmetry detector (Abingdon, UK), running with Aztec 9.0 Software. An EBSD map is shown in Figure 5a for the UK-RAFM. The EBSD maps in Figure 5 show IPFZ orientation, which highlights the martensitic structure, alongside a second map depicting grain boundaries grouped by misorientation angle to emphasise the prior-austenite grain (PAG) structure. The samples were orientated such that images are in the rolling direction (RD)–normal (N) plane. PAG sizes were estimated by first reconstructing the PAGs in MATLAB using MTEX and ORTools [60,61], and then calculating the area-weighted median grain size. The UK-RAFM has a PAG size ~14 µm (equivalent circle diameter), which is comparable to the 11–16 µm PAG size that is reported for early heats of Eurofer97 [36], but coarser than the more recent Eurofer-97 batch-3 (5–7 µm) [53]. Further analysis is being conducted to determine how variable the PAG size is across the ingot.

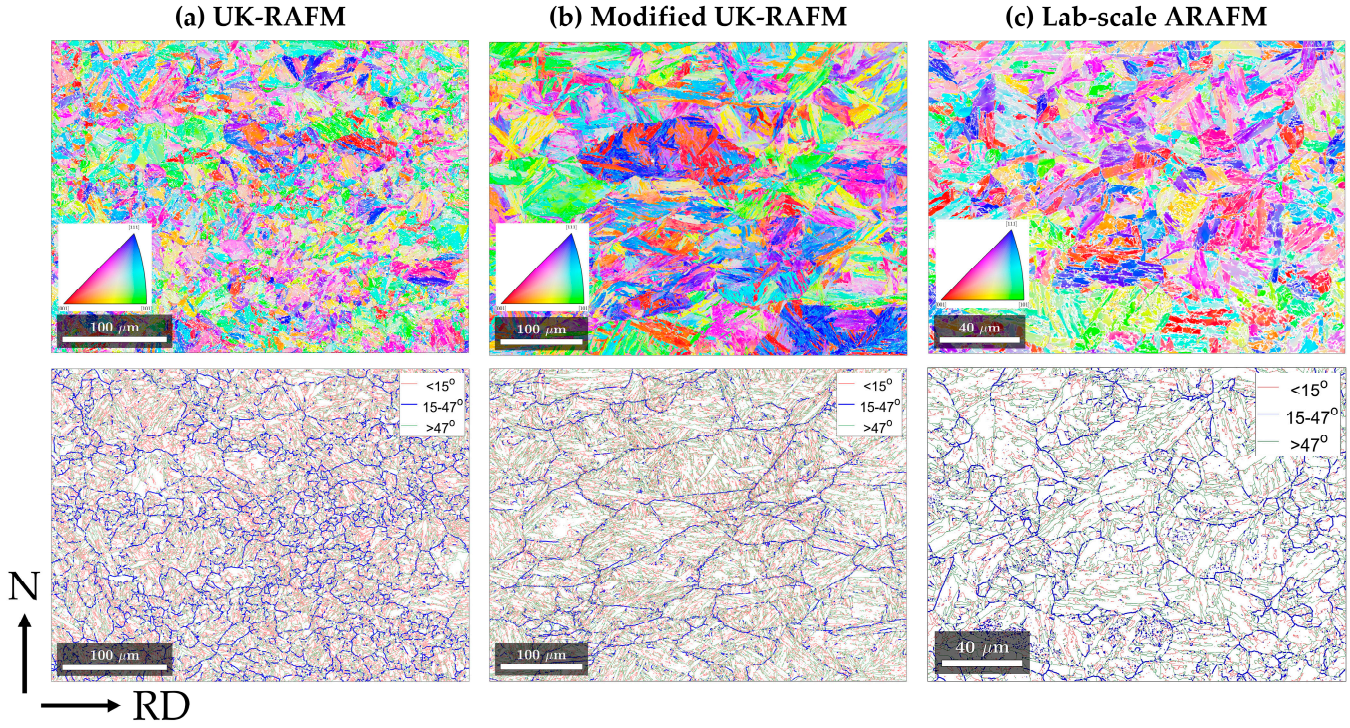

Figure 5. EBSD IPFZ orientation maps (**top**) and grain boundary misorientation maps (**bottom**) for; (**a**) UK-RAFM, (**b**) Modified UK-RAFM and (**c**) Lab-scale ARAFM. Reference direction used for images indicated in the bottom left (N = normal direction, RD = rolling direction). The grain boundary misorientation maps emphasise the prior austenite grain boundaries (thick blue lines). The lath boundaries (red and green) are shown for reference and not utilised here for subsequent analysis.

Transmission electron microscopy (TEM), both conventional and scanning (STEM), was carried out on the RAFM alloys, to study the precipitates. The JEOL NEOARM TEM (Tokyo, Japan) at the UKAEA, Materials Research Facility (MRF) was used for this. Samples were prepared as either twin-jet electropolished TEM discs or carbon extraction replicas. Figure 6a shows a dispersion of precipitates in the UK-RAFM alloy. Large $M_{23}C_6$ carbides decorate PAG boundaries, while smaller $M_{23}C_6$ decorate lath boundaries inside of the PAG. Energy-dispersive X-ray spectroscopy (EDS) highlights the chromium-rich $M_{23}C_6$ phases, alongside Ta and V enriched regions, indicative of TaC and VN (Figure 6b).

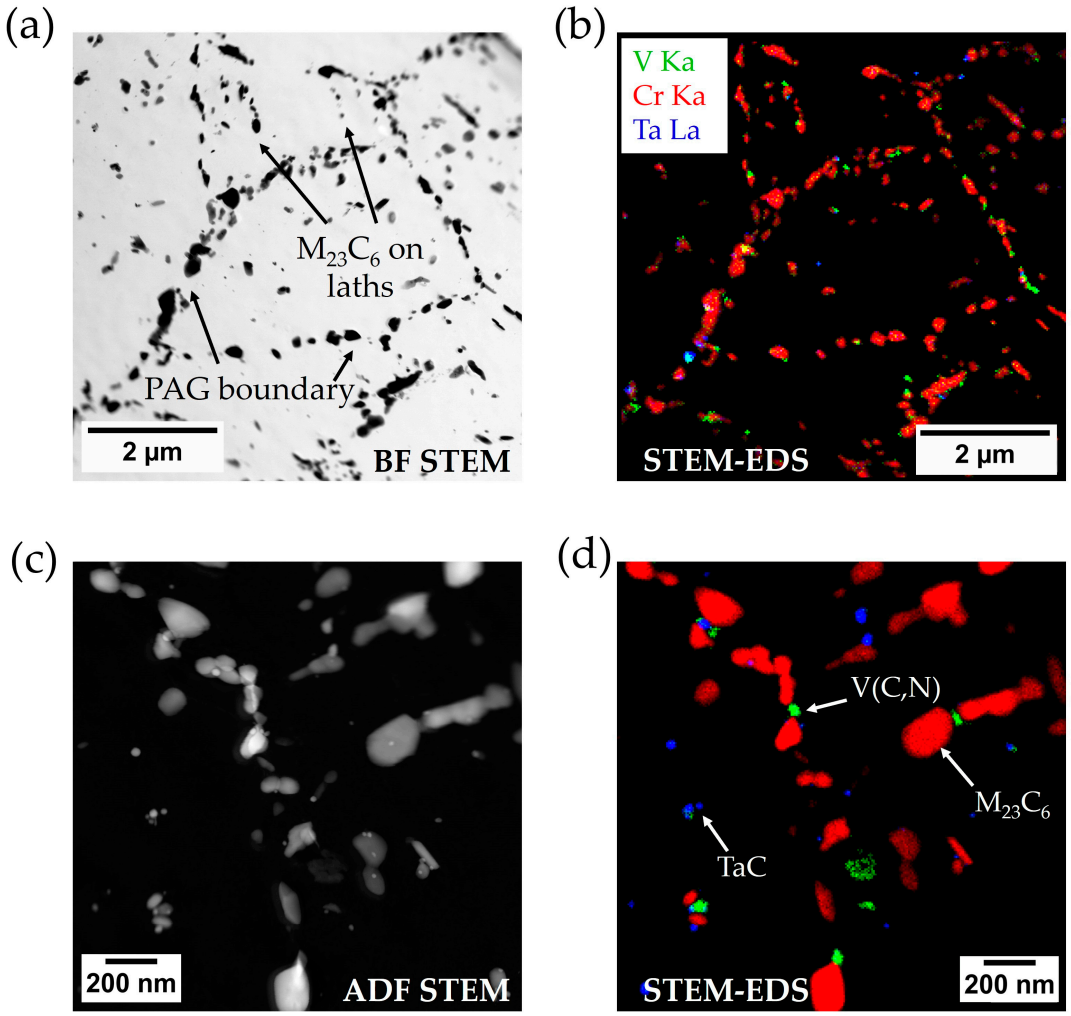

Figure 6. STEM analysis of the UK-RAFM steel, showing; (**a**) bright field (BF) STEM and precipitate network decorating grain boundaries; (**b**) combined STEM-EDS signal highlighting the presence of V (green), Cr (red) and Ta (blue) rich precipitates in the same region as the BF image; (**c**) higher magnification annular dark field (ADF) STEM image with corresponding STEM-EDS image (**d**).

Annular dark field (ADF) was used to assess a region of UK-RAFM at greater magnification (Figure 6c) which indicates that some finer precipitates may be enveloped by larger ones. Whilst difficult to fully corroborate in the STEM-EDS analysis of the same region, it appears that the V and Ta-rich precipitates could be nucleating at co-located sites (Figure 6d). Further evidence of this is shown in Supplementary Figure S1. This suggests that the high-temperature MX precipitates could be acting as nucleation sites for the $M_{23}C_6$ precipitates.

Measurements of the UK-RAFM precipitates indicate that the VN and TaC are approximately 20–50 nm in diameter, which is expected for a steel like Eurofer97 where such precipitates are typically on the order of 10 nm in size [62]. The $M_{23}C_6$ precipitates measure ~80–120 nm in diameter in the UK-RAFM steel and are located along the PAG boundaries, comparable to Eurofer97 [62]. The STEM precipitate analysis provides confidence that the UK-RAFM demonstrates a microstructure morphology which is analogous to Eurofer97.

Understanding the phase evolution within the UK-RAFM is useful for understanding the observed microstructures. Thermo-Calc 2024b software with the TCFE12 steel database was used to perform this analysis. A one-axis simulation was performed, stepping the temperature from 2000 °C to 200 °C to model the transformation behaviour and phase stability across this range. The volume fraction of phases was plotted for the UK-RAFM

(Figure 7a). Additionally, the amount of phase in the component was determined and plotted specifically for the VN and TaC precipitate phases to identify their elemental composition. Critical transformation temperatures (A1, A3, A4), the austenite phase field (A3 to A4), and the temperature window between MX dissolution and A4 were also extracted, shown in Table 2. This window is crucial for dissolving all MX-forming elements (Ta, V), therefore avoiding excessive coarsening of MX precipitates during subsequent heat treatment, whilst avoiding the delta ferrite field marked by A4.

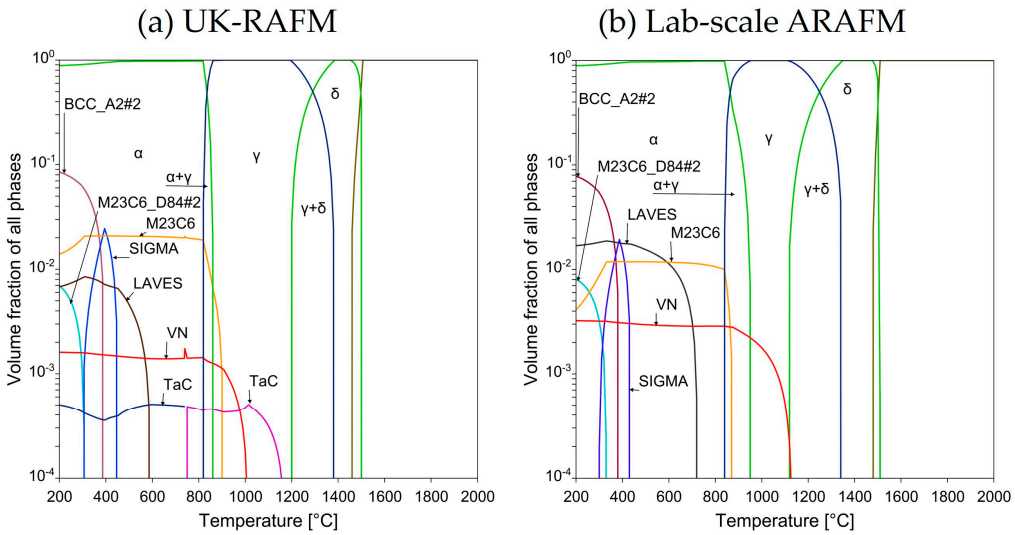

Figure 7. Thermo-Calc phase diagrams for; (**a**) UK-RAFM and (**b**) Lab-scale ARAFM.

Table 2. Phase boundaries and MX precipitate dissolution temperatures determined from Thermo-Calc simulations of UK-RAFM and Lab-scale ARAFM, all reported in °C.

Alloy Name	A1	A3	A4	A3 to A4 Window	VN Dissolution	TaC Dissolution	MX Dissolution Window
UK-RAFM	819	862	1194	332	1014	1175	19
Lab-scale ARAFM	839	953	1110	157	1134	-	−24

The UK-RAFM, with a higher than specified chromium (Cr) content of 10.1 wt.% (strong ferrite stabiliser), exhibited an A3 temperature of 862 °C and A4 of 1194 °C, providing an austenite phase field of 332 °C. This reflects a broad austenite stability range due to the high C content in this alloy. The solution treatment at 1200 °C should allow both MX phases to be fully dissolved before processing the alloy. The lower formation temperature of $M_{23}C_6$ compared to VN and TaC would explain the observation of co-precipitation of this phase alongside MX precipitates (Figure 6c,d), which act as nucleation sites, forming at much higher temperatures.

3.3. UK-RAFM Mechanical Performance

UK-RAFM mechanical test pieces were machined from the 14 mm plate, with sample test axes aligned with the rolling direction. The UK-RAFM alloy underwent tensile testing at Swansea University using round samples with a parallel gauge length of 27.5 mm and a diameter of 4 mm. An Instron 1361 100 kN electric screw testing machine (Norwood, MA, USA) with a strain rate of 0.00025 s^{-1} was used for all tests. A 24.5 mm extensometer was used initially and switched to crosshead displacement later in the test due to extensometer runout. Tests were carried out at room temperature and 650 °C, with

3 repeats per condition. Test results were compared to Eurofer97, with data derived from the literature [1,36] and discussed subsequently. Tensile tests were carried out in accordance with BS EN ISO 6892-1:2019 (RT) and BS EN ISO 6892-2:2018 (650 °C).

The results shown in Figure 8 demonstrated a slight increase in the strength of the UK-RAFM compared to Eurofer97. At room temperature (RT), compared to Eurofer97, UK-RAFM exhibited a 15.8 MPa increase in yield strength (YS) and 43 MPa increase in ultimate tensile strength (UTS). Interestingly, despite the increased strength of the UK-RAFM alloy, the uniform elongation (UE) is increased by 1.2 %pt. compared to Eurofer97, whilst the total elongation (TE) is reduced, as expected, by 2.4 %pt. However, the UK-RAFM alloy still offers a TE of 19.6%, comparable to Eurofer97 (22%) and F82H (21.5%) [63]. Testing at 650 °C (Figure 8) revealed that the UK-RAFM maintained its strength advantage with both the YS and UTS, 47.3 MPa and 31.6 MPa greater, respectively, than Eurofer97. Both UE and TE trend slightly lower as anticipated, 0.1 %pt. and 4.0 %pt. lower than Eurofer97, respectively. The tensile stress–strain curves used to derive the data for the UK-RAFM are shown in Supplementary Figure S2a,c.

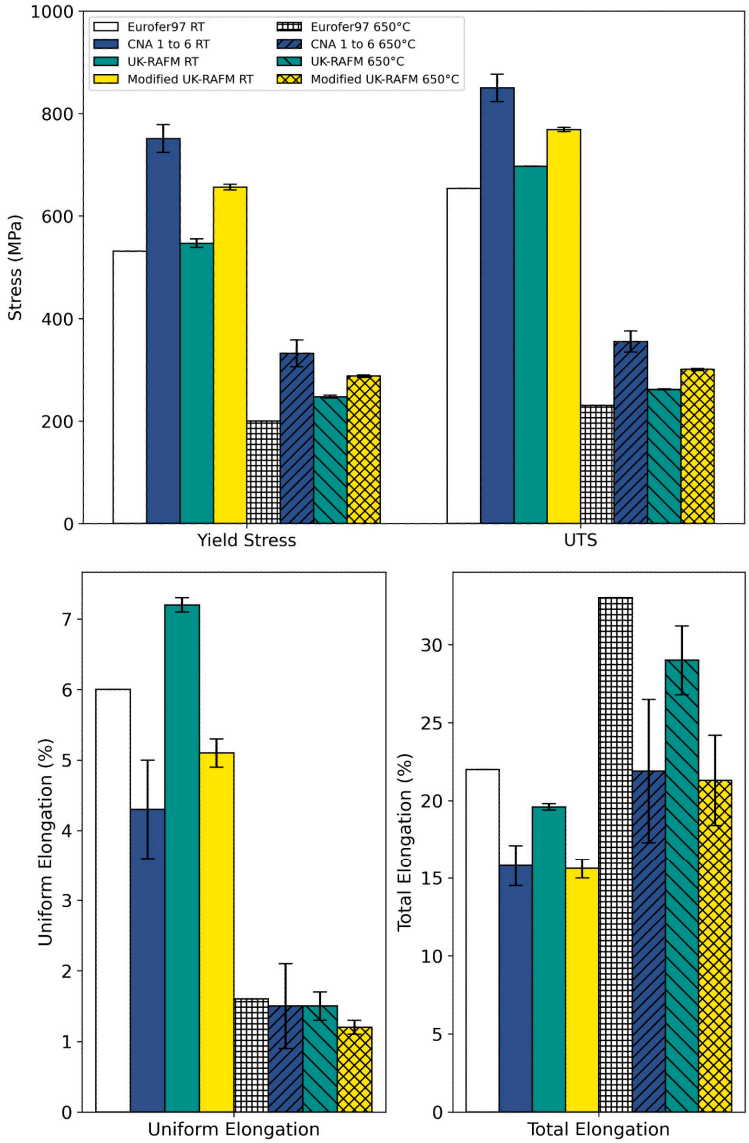

Figure 8. Tensile test results comparing Eurofer97 performance reported in the literature [1,36], alongside the average performance of CNAs 1 to 6 [18] with the UK-RAFM and Modified UK-RAFM. Yield strength (**top left**), ultimate tensile strength (**top right**), uniform elongation (**bottom left**) and total elongation (**bottom right**) are reported.

Clearly, compared to Eurofer97, the UK-RAFM offers a slight improvement in strength with a minor degradation in elongation. The strengthening elements measured within the UK-RAFM (Table 1) are not significantly different to Eurofer97, with W, V, N, and C all remaining within the specification (with the exception of Ta, which is 0.008 wt.% lower than the minimum bound for Eurofer97). Si is the most significantly out of specification element within the UK-RAFM alloy, nearly three times the limit specified for Eurofer97, whilst Ni at 0.02 wt.% is double the Eurofer97 specification and Cr is 0.615 wt.% above the maximum limit for Eurofer. Zhang et al. [64] showed general agreement with the proposed Si strengthening regression equation in 9Cr steel:

$$\sigma_s Si = 83.2 \times (\text{mass\% Si}) \text{ (MPa)} \quad (1)$$

According to Equation (1), assuming a Si content of 0.05 wt.% in Eurofer97 (Table 1), at room temperature, this would offer a solution strengthening contribution to the YS of 4.16 MPa. In the case of UK-RAFM, with 0.2 wt.% Si (Table 1), the solution strengthening contribution to the YS increases to 12.23 MPa, an 8.07 MPa increase over Eurofer97. This does not fully account for the 15.8 MPa increase in YS observed in the UK-RAFM, and other elements were less significantly out of specification. As strengthening effects are coupled with other microstructural features, it is difficult to conclude that chemical differences are solely driving the enhanced strength observed in the UK-RAFM alloy.

The TMT used for UK-RAFM may be the driving force behind the change in mechanical performance compared to Eurofer97, but this is difficult to definitively comment on. This is namely because the forging step and pre-processing steps used for Eurofer97 are not shared, and therefore the UK-RAFM forging step likely differs. This potentially is driving the change in mechanical performance manifested here.

Charpy Impact toughness of the UK-RAFM was assessed using a Zwick Roell RKP 450 J pendulum impact tester (Ulm, Germany) at Imperial College London (ICL), in accordance with ASTM E23. These data, as seen in Figure 9a, showed that the UK-RAFM has an upper shelf energy (USE) of 200J, 70J lower than Eurofer97 [36]. The DBTT is increased to −40 °C in UK-RAFM compared to Eurofer97, which has a DBTT ranging from −53 °C to −70 °C [36]. These observations further indicate that the increased strength of UK-RAFM has led to additional embrittlement of the alloy. The implications for this in an operational context remain to be seen, as the testing of irradiated material is required to ascertain the extent of any DBTT shift to higher temperatures compared to other RAFM steels.

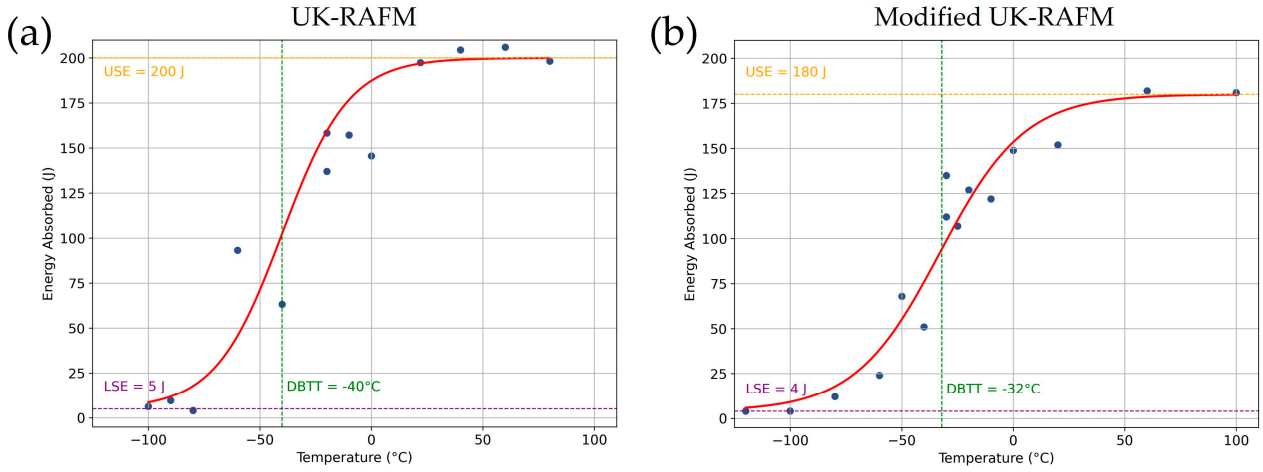

Figure 9. Charpy impact toughness results for (**a**) UK-RAFM, and (**b**) Modified UK-RAFM as a function of temperature. Lines of best fit are overlaid in red.

The creep performance of the UK-RAFM alloy was assessed at ICL using a Zwick Roell Lever Arm rig (Ulm, Germany) in accordance with BS EN ISO 204:2023 and ASTM E139-24. A preliminary test at 650 °C using an applied stress of 90 MPa was conducted. The creep data is plotted alongside other RAFM, CNA, and ferritic–martensitic steels, and is shown in Figure 10. The UK-RAFM provided a creep lifetime of 2157 h, a ~1.6× improvement in performance compared to Grade 91 steel under identical conditions. The UK-RAFM also exceeds the creep performance of comparable RAFM steels in this class, such as Eurofer97 and F82H, by ~3.9× and ~1.7×, respectively, and is comparable to the CNAs. However, the performance of Grade 92 steel under these conditions exceeds the UK-RAFM by ~4.8×. In this case, Grade 92 is regarded as a "gold standard" for target performance and this level of performance is being sought within the range of future NEURONE ARAFM alloys being developed.

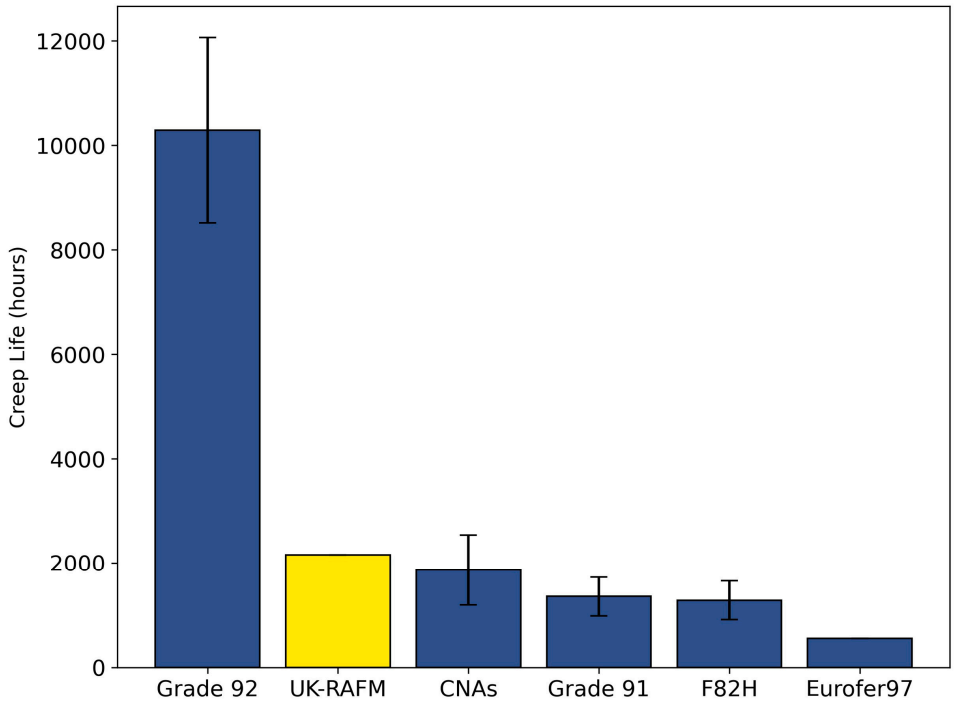

Figure 10. Creep performance at 650 °C and 90 MPa applied stress for UK-RAFM (shaded yellow) in comparison to FM steels (Grade 92 [65,66], Grade 91 [67]) and the RAFM steels F82H [63], Eurofer97 [36], and inferred performance of the CNAs reported in [18]. The error bars show one standard deviation.

4. Enhancing Alloy Performance for Fusion Plant Structural Applications

4.1. Application of a Modified TMT to UK-RAFM

One section from the UK-RAFM billet underwent an adapted TMT process, producing an additional 14 mm plate. This TMT process was designed to demonstrate how alloy production enhancements developed in NEURONE could be used to improve the high temperature properties of base RAFM chemistry steels. These plates were processed using the following TMT parameters: initial forging at 1170 °C to 48% reduction, before re-heating to 1170 °C for a multi-pass rolling schedule for a ~60% reduction to 14 mm plate thickness and a FRT of 950 °C. Detailed specifics associated with the rolling schedule are commercially sensitive and cannot be fully disclosed at this time. Finally, the plates were tempered at 760 °C for 90 min, followed by air cooling. This heat treatment aimed to achieve better MX precipitate dissolution, combined with a grain-refining thermomechanical treatment. The final passes below the non-recrystallisation temperature (TNR) typically produce a

pancaked grain structure where the high dislocation density provides a high density of nucleation sites for subsequent precipitation. The alloy produced as a result here is referred to as Modified UK-RAFM.

The Modified UK-RAFM underwent EBSD analysis using the same methodology as described for the UK-RAFM, shown in Figure 5b. The Modified UK-RAFM shows the pancaked grain structure that had been expected from including a final rolling temperature (FRT) below the TNR. The grains show preferable elongation in the RD. In addition, the Modified UK-RAFM has a larger grain size of 75 μm (in the RD) compared to the UK-RAFM (14 μm). Again, this is due to the rolling schedule which took the alloy through a FRT below the TNR, preventing any further grain refinement.

4D-STEM analysis was carried out using an FEI Talos (Hillsboro, OR, USA) with a Quantum Detectors Merlin direct electron detector (Harwell, UK). This approach allowed for a composite image to be generated showing all precipitates present in the material that produce Bragg scattering distinct from the matrix, in a range of orientations, rather than being constrained to a single reflection as is the case with conventional TEM diffraction imaging. Additionally, it is possible to subtract the incoherent 'background' scattering from these images, which increases the precipitate signal to noise ratio and produces clearer images [68]. Images taken down the [100] zone axis show multiple orientations of the VN precipitates simultaneously. Diffraction patterns of the precipitates in Figure 11e–g show typical VN orientation relationship with the matrix with the (200) planes of both precipitates parallel to each other.

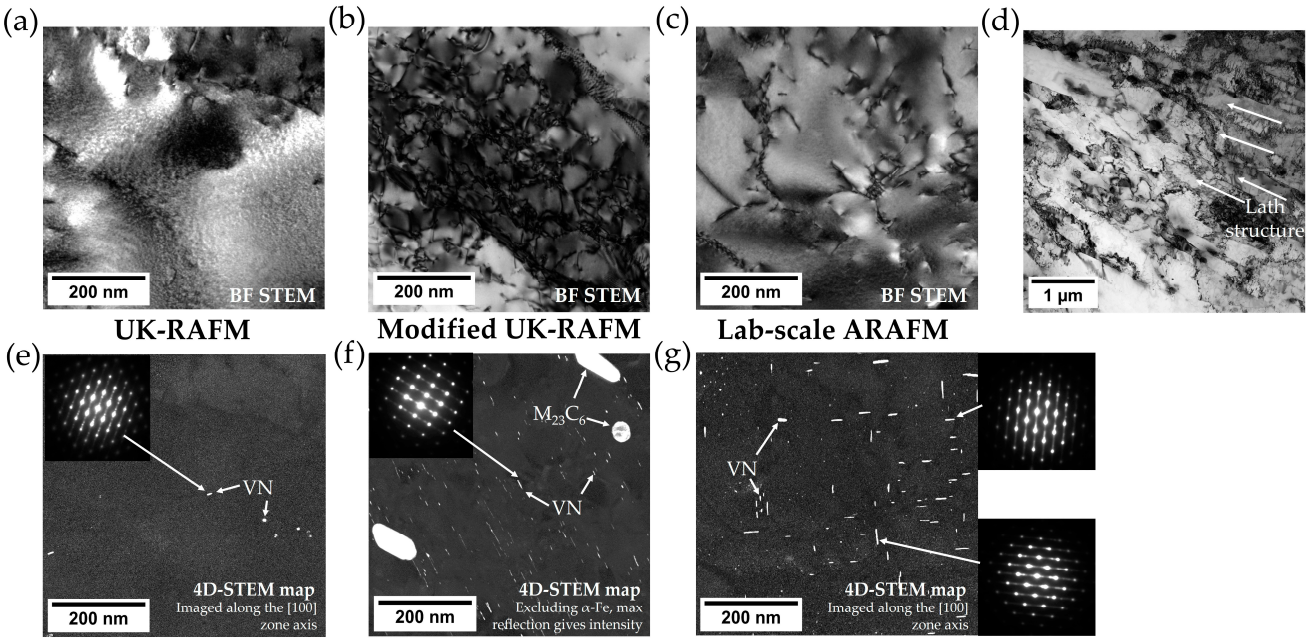

Figure 11. TEM micrographs showing (**a**) and (**e**) bright-field STEM and 4D-STEM images, respectively, of the UK-RAFM alloy, viewed down the [100] zone axis; (**b**) and (**f**), bright-field STEM and 4D-STEM images, respectively, of the Modified UK-RAFM alloy, viewed down the [110] zone axis; (**c**) and (**g**) bright-field STEM and 4D-STEM images, respectively, of the Lab-scale ARAFM alloy, viewed down the [100] zone axis. Frame (**d**) shows a larger field of view for (**b**) highlighting the typical lath structures within the alloy. Diffraction patterns in e-g are taken by integrating the patterns over the VN precipitates. Where 2 orientations of precipitate are visible in (**g**) two separate diffraction patterns are displayed.

Images collected along the [100] and [110] zone axis are shown in Figure 11. Clearly, the Modified UK-RAFM benefits from a higher VN density (Figure 11f) compared to the UK-RAFM (Figure 11e). In the case of the UK-RAFM, and Modified UK-RAFM, the precipitate

densities were found to be 1×10^{20} m^{-3} and 2.2×10^{22} m^{-3} respectively. This demonstrates how the application of the TMT to UK-RAFM has yielded a significant (220-fold) increase in the precipitate number density.

The Modified UK-RAFM offered a surprising boost in tensile performance compared to the UK-RAFM alloy. Once again, tests were carried out on the Modified UK-RAFM using an Instron 1361 100kN electric screw testing machine (Norwood, MA, USA) at Swansea University, using identical sample sizes to the UK-RAFM and an identical strain rate of 0.00025 s^{-1}. Three repeat tests were conducted at both room and elevated temperatures. Compared to the UK-RAFM, as shown in Figure 8, the modified UK-RAFM offers an increase in YS and UTS of 109.6 and 71.6 MPa (20% and 10%), respectively, at RT. This is coupled with a reduction in UE and TE of 2.1 %pt. and 4.0 %pt., respectively. At 650 °C compared to UK-RAFM, the Modified UK-RAFM offers an increase in YS and UTS of 40.1 MPa and 38.9 MPa (16% and 15%), respectively. Compared to Eurofer97, this is a 44% increase in YS and 31% increase in UTS at 650 °C. The Modified UK-RAFM suffers a reduction in ductility compared to UK-RAFM when tested at 650 °C, −0.3 %pt. and −7.7 %pt. of UE and TE, respectively. This boosted mechanical performance after utilisation of a multi-pass rolling TMT is a clear example of how alloy process optimisation can be used to deliver enhanced strength, despite no change in the alloy chemistry. The tensile stress–strain curves used to derive the data for the Modified UK-RAFM are shown in Supplementary Figure S3. It should be noted that during testing, a slippage of the extensometer occurred, resulting in a switch to crosshead displacement being used for ascertaining strain instead.

Charpy impact testing (Figure 9b) reveals a reduction in the Modified UK-RAFM impact toughness properties, with the USE decreasing to 180 J (20 J, or 10% reduction compared to UK-RAFM). The DBTT shifts upwards to −32 °C compared to UK-RAFM (an 8 °C increase). At the time of writing, the Modified UK-RAFM alloy was undergoing creep testing. These data will be reported in a future publication.

4.2. Development of a Lab-Scale ARAFM Prototype Alloy

In the next phase, it was of interest to apply the NEURONE TMT to a customised alloy chemistry. In particular, enhancement of W content to encourage solution strengthening (targeting 2.0 wt.%), and an emphasis on VN formation were adopted for the Lab-scale prototype. The approach to favour VN follows an investigation by Puype et al. [69], who showed a strong correlation to VN formation as a function of V addition to the alloy, whilst further Ta additions failed to yield a further increase in TaC. Hence, removal of Ta and emphasis on VN formation was designated as a primary strategy for this alloy. Otherwise, Eurofer97 base chemistry was used as a basis to develop the target Lab-scale ARAFM alloy composition (shown in Table 1), conformant to the reduced-activation design methodology. This alloy was produced at the Swansea University MACH1 (Materials Advanced Characterisation Centre) laboratory. The alloy presented here is analogous to "Alloy-1" (9Cr-2W-VTa) previously discussed by Haley et al. from an irradiation resilience perspective [47], and more recently by Gibson et al. [68].

As part of the MACH1 rapid alloy prototyping (RAP) capabilities, centrifugal casting was used to produce the ingot, with a resultant size of 40 mm × 55 mm × 8 mm and a mass of 140g. Induction heating was used to melt solid precursor elements in a ceramic crucible. Iron, Cr, Mn, V, Ta, and C were added in high purity form. Nitrogen and W were introduced using FeCrN and FeW master alloys, respectively. Once fully molten, the material was cast into a copper mould. The Lab-scale ARAFM then underwent normalisation at 1100 °C before rolling from 1015 °C to a FRT of 820 °C to achieve a 45% reduction. The alloy was then isothermally treated at 900 °C for 20 min, to produce an increased number density

of refined MX precipitates [32,33,35]. In principle, this stage should also enable PAG refinement to enhance the toughness of the alloy. Finally, a temper step at 750 °C for 45 min was carried out. A small ~3 mm-thick plate was produced as the result. Resultant compositions were measured using a SpectroLab LACM12 OES (Kleve, Germany). At least 12 measurements were made on the plate and the actual Lab-scale ARAFM composition is reported in Table 1. Due to the increased N and Ni content in the Lab-scale ARAFM, the FISPACT-II activation profile (Figure 4) is slightly worsened compared to Eurofer97 and UK-RAFM. The Lab-scale ARAFM activity after 100 years after shutdown was calculated to be 226 MBq/kg. The time to reach an acceptable dose rate for hands-on processing is 15 years, comparable to UK-RAFM.

Thermo-Calc assessment of the Lab-scale ARAFM was conducted using the established OES composition and identical method as applied in the case of the UK-RAFM alloy. The analysis indicated that the Lab-scale ARAFM proves difficult to normalise effectively due to the VN dissolution temperature of 1134 °C, reported in Table 2. This is higher than the A4 (delta (δ)-ferrite phase) boundary of 1110 °C (Table 2), preventing complete dissolution of VN during normalisation, without potentially forming δ-ferrite. Therefore, as is visible in Figure 7b, normalisation was conducted right upon the A4 boundary at 1110 °C which would not be ideal during upscaled processing of this alloy. Therefore, future ARAFM alloy iterations will seek to widen the MX dissolution temperatures and A4 boundary, to enable normalisation in the fully austenite phase field to be achieved.

EBSD analysis of the Lab-scale ARAFM alloy, conducted in the same way as outlined for the UK-RAFM variants, is shown in Figure 5c. These revealed the familiar martensitic structure, as anticipated. In the case of the Lab-scale ARAFM, which is rolled above the TNR, as is usual for alloys like Eurofer97, an equiaxed grain morphology is observed. A PAG size of 20 µm was observed, which is slightly coarser than the 14 µm established for the UK-RAFM alloy, but in the range typical for Eurofer97 [36]. Compared to the Modified UK-RAFM, which had a FRT below the TNR, the Lab-scale ARAFM exhibited finer PAG sizes. This is likely due to the higher initial normalising temperature of the Modified UK-RAFM compared to the Lab-scale ARAFM (1170 °C vs. 1100 °C).

4D-STEM analysis of the Lab-scale ARAFM was carried out using FEI Talos (Hillsboro, OR, USA) with a Quantum Detectors Merlin direct electron detector (Harwell, UK). A lamella was imaged using 4D-STEM (Figure 11c,g), which shows VN precipitates with a needle-like morphology. The VN precipitates in the Lab-scale ARAFM (Figure 11g) appear to be coarser than those present in the Modified UK-RAFM alloy (Figure 11f). This is possibly an effect of the non-optimal VN dissolution temperature to A4 boundary identified in the Thermo-Calc analysis. Without complete dissolution of the VN, coarsening would be expected to occur during subsequent TMT steps. This is in contrast to the Modified UK-RAFM which had a more optimal processing window (Figure 7a and Table 2) and hence produced a finer VN distribution due to their complete dissolution during processing. However, the number density of precipitates is increased substantially in the Lab-scale ARAFM, at 5.4×10^{21} m^{-3}, a 54-fold increase compared to the UK-RAFM.

Due to the limitations associated with the small-scale casts using RAP, tensile tests of the Lab-scale ARAFM were carried out independent to the UK-RAFM alloy. Flat geometry Lab-scale ARAFM tensile specimens measuring with a 40 mm parallel length, 6 mm gauge width and thickness of 2 mm were extracted from the plate. Tensile tests were carried out at Swansea University, at a temperature of 600 °C, using a Phoenix 25 kN thermophysical fatigue machine (Brierley Hill, UK) and a strain rate of 0.00025 s^{-1}. Due to the limitations of the test rig, these tests were limited to 600 °C, so a comparison to the UK-RAFM alloy at 650 °C was not possible. The tensile stress–strain curve used to derive the Lab-scale ARAFM data is shown in Supplementary Figure S4.

The UK-RAFM alloy was tested at Imperial College London, using a Mayes DM200 (Windsor, UK) at 600 °C and a strain rate of 0.00025 s^{-1}. The sample geometry used had a gauge length of 40 mm parallel gauge length and a diameter of 7 mm. The extensometer used had a width of 12.5 mm. Figure 12 shows the Lab-scale ARAFM performance compared to UK-RAFM and Eurofer97 (from the literature). The tensile stress–strain curve used to derive the UK-RAFM data is shown in Supplementary Figure S2b. Unfortunately, test data for the Modified UK-RAFM at 600 °C was not available for direct comparison. In all cases, only a single test was conducted at this condition, hence errors are not reported at this time.

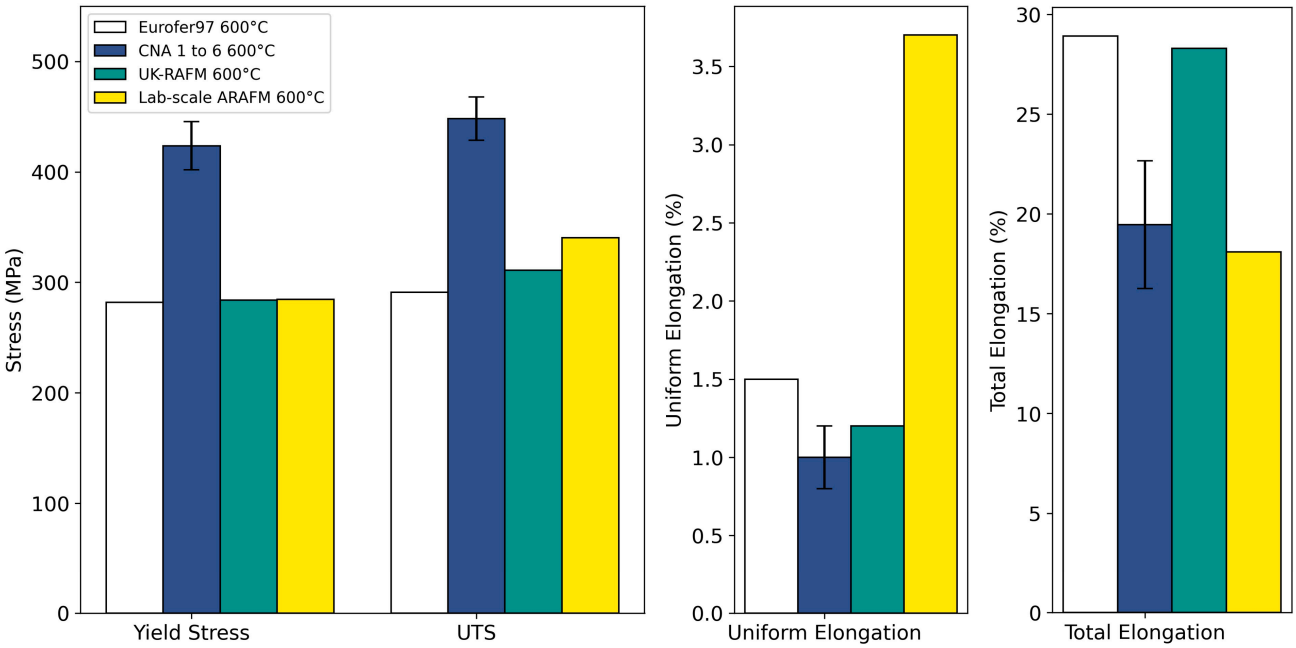

Figure 12. Tensile performance at 600 °C for Lab-scale ARAFM compared to CNAs 1 to 6 [18], Eurofer97 [36], and UK-RAFM.

The Lab-scale ARAFM demonstrated a YS almost identical to the UK-RAFM alloy (comparable to Eurofer97). However, its UTS of 340.5 MPa exceeded both UK-RAFM and Eurofer97, by 9% and 17%, respectively. In addition, the UE of the Lab-scale ARAFM offers nearly 2.5× increase over Eurofer97. However, the Lab-scale ARAFM TE was the lowest compared to both Eurofer97 and the UK-RAFM, at just 18.1%. It is important to note that the Lab-scale ARAFM tensile tests utilised sub-size samples, compared to standard geometries. The CNAs on the other hand, demonstrated superior strength compared to the Lab-scale ARAFM (both YS and UTS above 400 MPa). However, the elongation properties were more of a mixed picture, with the Lab-scale ARAFM offering superior UE and equivalent TE to the CNAs.

The significant reduction in TE observed in the Lab-scale ARAFM could be explained by a few factors, including strain rate, sample size, and geometry effects. In this study, a consistent strain rate was used for all tensile tests and therefore can be eliminated as a cause. Smaller, non-standard samples exhibit a higher TE and also a higher degree of scatter, making it difficult to compare to standard sized samples [70]. The slimness ratio also influences the TE, with an increasing slimness ratio, the TE will decrease. Both samples had a comparable slimness ratio, with 8.66 and 6.45 for ARAFM and UK-RAFM, respectively. This difference is not expected to give a drastic change in TE [70]. The biggest difference between the Lab-scale ARAFM and UK-RAFM is the sample geometry. The ARAFM sample was tested using a flat sample, while the UK-RAFM was round. In general,

both flat and round samples respond in a similar fashion during the stress–strain curve up until the UTS [71]. Once necking takes place, the two sample geometries behave differently. Round samples have a more uniform stress distribution compared to flat samples [71]. The UK-RAFM round sample was also thicker, which enhances the amount of necking before fracture. Sharp corners on the flat samples act as stress raising features, resulting in a non-uniform stress distribution, leading to more pronounced strain localisation, which can result in rapid, localised yielding and premature fracture [72]. Unfortunately, due to limitations acquiring more material, it was not possible to validate the Lab-scale ARAFM performance directly using identical tensile sample sizes and the same test rig.

5. Evolution of Alloy Performance

The UK-RAFM alloy, produced using an EAF and intended as an analogue for typical 9 wt.% Cr RAFM steels like Eurofer97, has demonstrated a surprising boost in tensile strength and creep lifetime compared to the conventional VIM + secondary processed RAFM counterparts. Whilst the minor deviations in UK-RAFM chemistry are not believed to strongly influence the alloy mechanical performance, the variance in the initial pre-treatment of the alloy by way of forging could be producing this performance boost. As the methodology used to produce Eurofer97 is not widely available, a 50% reduction forging step immediately following the 1200 °C solution anneal appears the likely cause. The low precipitate density observed in the UK-RAFM (Figure 11d), at a comparable level to Eurofer97, indicates that the strengthening mechanisms lie elsewhere within the microstructure, which requires further investigation. The gains in strength and creep lifetime within the UK-RAFM are tempered by reductions in ductility and impact toughness compared to Eurofer97, which require further assessment to ensure acceptable and safe operation of components constructed from this alloy can be maintained. The UK-RAFM maintains a low residual activity after 100 years of decay, with a comparable activation profile to Eurofer97 (Figure 4). However, the broadly successful performance of the UK-RAFM alloy, from a mechanical, microstructural and radiological perspective gives confidence that EAF upscaling for RAFM steels is a viable route forward, towards commercial fusion plant operation.

The application of TMTs to the Modified UK-RAFM, involving multi-pass rolling, yielded an alloy with a visibly different base microstructure compared to the UK-RAFM (Figure 5). Larger, more pancaked grains are visible due to the FRT below the TNR. The primary outcome of this TMT however, was to demonstrate how the alloy performance could be improved further through the application of a bespoke processing schedule. Once again, the Modified UK-RAFM demonstrated enhanced strengthening compared to UK-RAFM during tensile tests, particularly at 650 °C (Figure 8). As is the usual compromise, however, YS and UTS rose at the expense of UE and TE. However, the loss of UE in the Modified UK-RAFM was only marginal, at 0.3 %pt. lower compared to UK-RAFM. Given the intended operation of components, well below the UTS, this performance is very promising from an engineering standpoint. The 220-fold increase in precipitate density of the Modified UK-RAFM compared to UK-RAFM (Figure 11) is likely one of the primary contributing factors to this improved performance.

The Lab-scale ARAFM combined a modified chemistry favouring VN formation, and a TMT which utilised a precipitate hold step to encourage a higher density of VN to form. The UTS at 600 °C was observed to be superior to the UK-RAFM, an indication that the combination of alloy chemistry and TMT optimised for MX precipitate formation have contributed to the strength of the alloy. Interpretation of alloy ductility is difficult in the case of the lab-scale ARAFM, due to the sub-size samples used and different sample geometries, influencing the results.

One of the challenges when developing RAFM steels, where many austenite stabilisers are removed, is maintaining a sufficiently wide processing window, in the austenite phase field. The reasons for this are twofold. Firstly, to ensure that ausforming can begin at sufficiently high temperatures to enable complete dissolution of MX precipitates, reducing the concern of over-coarsening (which would negatively impact alloy toughness and creep life). Secondly, the A4 (δ-ferrite) formation temperature must be high enough to enable an achievable processing window, bounded at the lower end by the MX dissolution temperature. If these temperatures are too close, the formation of deleterious delta-ferrite may be unavoidable, or MX precipitates may over-coarsen. In the case of the Lab-scale ARAFM, the processing window predicted by Thermo-Calc (Figure 7 and Table 2) raised concerns that complete dissolution of the VN would not be possible, potentially limiting the scale of fine precipitates that could be evolved in the alloy. Future iterations of the ARAFM will need to emphasise a widening of this processing window, to ensure a fully optimised MX morphology and number density is achieved. The Lab-scale ARAFM is a starting point for future research, with significant further optimisation required and further developments will be reported on in future.

The benefits of the isothermal treatment step, included in the TMT for the Lab-scale ARAFM are therefore inconclusive. This is particularly the case when compared to the Modified UK-RAFM which lacked the precipitation treatment step but produces a higher density of fine precipitates when imaged using 4D-STEM (Figure 11). It may be that due to the lack of optimisation of the MX dissolution and A4 processing window, that the precipitates in the Lab-scale ARAFM were able to coarsen excessively, at the expense of number density, limiting their effectiveness at enhancing strength within the final alloy.

6. Conclusions

The use of EAF to produce a 5.5 tonne continuous cast RAFM steel billet has been demonstrated. After rolling into plate, the UK-RAFM alloy demonstrated superior tensile strength and creep life compared to Eurofer97, and an acceptable reduced activation profile despite some deviations from the chemical specification. The increased strength and creep properties of the UK-RAFM compared to other RAFM alloys, like Eurofer97, offers the opportunity to run fusion plants at higher temperatures, for extended durations. Whilst the gains in strength and creep life of the UK-RAFM were notable, and in the latter case, exceeded the performance of conventional ferritic–martensitic Grade 91 steel, the precise reasons for this performance gain were not immediately evident. Due to the uncertainties associated with the Eurofer97 pre-processing steps, the performance enhancement of the UK-RAFM was attributed to the pre-treatment forging step; the only likely major departure from the Eurofer97 specification since the other heat treatment parameters used were identical. The utilisation of a modified TMT unlocked substantial further gains in strength. The modified UK-RAFM alloy, utilising a multi-pass rolling TMT schedule, offered superior strength during tensile testing. However, this is offset by reductions in UE and TE, which must be carefully balanced depending on the operating environment intended for the alloy. In addition, the Modified UK-RAFM suffered a reduction in USE and increased DBTT compared to the UK-RAFM counterpart, indicating reduced toughness as a result of the additional strengthening.

Whilst TMT optimisation has been shown to be crucial for fully exploiting enhanced strengthening in these alloys, chemical optimisations can also be sought for compound gains alongside the TMT. The combination of alloy chemistry and process optimisation towards ‘fusion-grade’ steels has been the focus of the NEURONE programme. An initial Lab-scale ARAFM steel exploiting VN formation has been explored. This has been coupled with an isothermal treatment step within the TMT schedule, theoretically enabling a greater

number density of MX precipitates to be evolved. Despite the increase in UTS observed in the ARAFM, the alloy composition likely requires further optimisation to allow for a wider separation between complete dissolution of the MX phases and the upper bound A4 temperature. In this study, whilst a substantial precipitate density was observed in the Lab-scale ARAFM, this was lower than the Modified UK-RAFM alloy which utilised standard Eurofer97-type chemistry.

Subsequently, the NEURONE programme has continued adapting and improving the ARAFM alloy series and this has culminated in an additional 5.5 tonne EAF billet being produced at MPI earlier this year. The design and performance of this alloy will be explored in a future publication. This integrated approach between optimising alloy composition to enhance the formation of required microstructural constituents, application of bespoke TMTs to drive high-strength performance, and working in tandem with industry partners to deliver these steels at scale via economically viable means, is now bearing fruit. The study outlined here paves the way for the production of a new series of low-cost RAFM steels, optimised for high-temperature applications within fusion power plants.

Supplementary Materials: The following supporting information can be downloaded at: https://www.mdpi.com/article/10.3390/jne7010001/s1. Figure S1. ADF-STEM images of the UK-RAFM alloy demonstrating the presence of MX phases near to, or within M23C6 (indicated by arrows). Figure S2. Stress strain curves from tensile tested UK-RAFM. Test temperatures were; (a) RT, (b) 600 °C and (c) 650 °C. Figure S3. Stress strain curves from the tensile tested Modified UK-RAFM. Test temperatures were (a) RT and (b) 650 °C. Note: that due to extensometer slippage, crosshead displacement was used part way through testing in (b) curve 1. Figure S4. Stress-strain curve from the tensile tested Lab-scale ARAFM at 600 °C. Table S1. Full alloy compositions, including impurity elements used for the FISPACT-II activation analysis.

Author Contributions: Conceptualization, D.B., J.H., S.J., N.L. and P.B.; Methodology, D.B., B.E., J.H., J.J., A.C., S.J., D.H., T.A., P.S., N.L., R.B., A.B., A.S. and P.B.; Software, B.E., S.J. and D.H.; Validation, B.E., J.H., J.J., S.J. and D.H.; Formal Analysis, D.B., B.E., J.H., A.C., J.J., S.J., D.H., T.A., P.S. and A.B.; Investigation, B.E., J.H., J.J., A.C., S.J., T.A., S.M., D.H., P.S. and A.B.; Resources, D.B., N.L., S.M., R.B., A.S. and P.B.; Data Curation, D.B., B.E., J.H., A.C., J.J., S.J., T.A., D.H., P.S. and A.B.; Writing—Original Draft Preparation, D.B., B.E., J.H., J.J., A.C., S.J. and D.H.; Writing—Review and Editing, D.B., B.E., J.H., J.J., S.J., D.H., N.L., P.S., R.B., A.B., A.S. and P.B.; Visualisation, D.B., B.E., J.H., J.J., A.C., D.H. and P.S.; Supervision, D.B., N.L., R.B., A.S. and P.B.; Project Administration, D.B., N.L. and R.B.; Funding Acquisition, D.B., N.L., S.M., R.B. and P.B. All authors have read and agreed to the published version of the manuscript.

Funding: This work has been funded by the NEUtron iRradiatiOn of advaNced stEels (NEURONE) programme via Fusion Futures. As announced by the UK Government in October 2023, Fusion Futures aims to provide holistic support for the development of the fusion sector. In addition, part-funding for this work has been provided by the EPSRC Energy Programme, grant number EP/W006839/1. The research used UKAEA's Materials Research Facility, which has been funded by and is part of the UK's National Nuclear User Facility and Henry Royce Institute for Advanced Materials. The Lab-scale ARAFM used in this study was developed with support from the Research Wales Innovation Fund Collaboration Booster, PROJECT #FF2.

Data Availability Statement: The data presented in this study may be available on request from the corresponding author. Due to the commercial sensitivity associated with the programme, full disclosure of underlying data may not be possible.

Acknowledgments: The authors would like to acknowledge input provided by Mark Gilbert at UKAEA, for assistance in providing the required libraries for FISPACT-II. The authors also thank Arunodaya Bhattacharya at the University of Birmingham for insightful discussions during the early phases of the NEURONE programme. In addition, the authors thank Alexandra Dickinson-Lomas, at UKAEA, who provided invaluable assistance preparing several samples for subsequent analysis

as part of this study. During the preparation of this manuscript, the authors used GPT-4/5 for the purposes of producing Python scripts for data analysis. The authors have reviewed and edited the output and take full responsibility for the content of this publication.

Conflicts of Interest: The authors declare no conflicts of interest.

Abbreviations

The following abbreviations are used in this manuscript:

ALAP	As low as possible
ARAFM	Advanced reduced-activation ferritic martensitic
BRAFM	Boron-strengthened reduced-activation ferritic martensitic
CNA	Castable nanostructured alloy
DBTT	Ductile to brittle transition temperature
EAF	Electric arc furnace
EBSD	Electron backscatter diffraction
EDS	Energy dispersive X-ray spectroscopy
EELS	Electron energy loss spectroscopy
ESR	Electro-slag remelting
FRT	Final rolling temperature
LLW	Low-level waste
LTHE	Low-temperature hardening embrittlement
MX	Metal carbonitride
NEURONE	NEUtron iRradiatiOn of advaNced stEels
ODS	Oxide dispersion strengthened
OES	Optical emission spectroscopy
PAG	Prior austenite grain
RAFM	Reduced-activation ferritic martensitic
RAP	Rapid alloy prototyping
RT	Room temperature
RTO	Research technology organisation
SEM	Scanning electron microscopy
STEM	Scanning transmission electron microscopy
STEP	Spherical Tokamak for Energy Production
TaC	Tantalum carbide
TE	Total Elongation
TEM	Transmission electron microscopy
TiC	Titanium carbide
TMT	Thermomechanical treatment
TNR	Temperature of non-recrystallisation
UE	Uniform Elongation
USE	Upper shelf energy
UTS	Ultimate tensile strength
VAR	Vacuum arc remelting
VIM	Vacuum induction melting
VN	Vanadium nitride
YS	Yield strength

References

1. Gaganidze, E.; Gillemot, F.; Szenthe, I.; Gorley, M.; Rieth, M.; Diegele, E. Development of EUROFER97 database and material property handbook. *Fusion Eng. Des.* **2018**, *135*, 9–14. [CrossRef]
2. Jitsukawa, S.; Tamura, M.; Van Der Schaaf, B.; Klueh, R.L.; Alamo, A.; Petersen, C.; Schirra, M.; Spaetig, P.; Odette, G.R.; Tavassoli, A.A.; et al. Development of an Extensive Database of Mechanical and Physical Properties for Reduced-Activation Martensitic Steel F82H. *J. Nucl. Mater.* **2002**, *307–311*, 179–186. [CrossRef]

3. Babu, M.N.; Prajapati, A.; Sasikala, G.; Albert, S.K.; Das, C.R.; Paul, T. Effect of Rolling Temperature on Fracture Properties of INRAFMS at Different Temperatures. *J. Mater. Eng. Perform.* **2018**, *27*, 4871–4880. [CrossRef]
4. Chun, Y.B.; Rhee, C.K.; Lee, D.W.; Park, Y.H. Enhanced high-temperature mechanical properties of ARAA by thermo-mechanical processing. *Fusion Eng. Des.* **2018**, *136*, 883–890. [CrossRef]
5. Huang, Q. Status and improvement of CLAM for nuclear application. *Nucl. Fusion* **2017**, *57*, 086042. [CrossRef]
6. Cane, J.; Barth, A.; Farrington, J.; Flynn, E.; Kirk, S.; Lilburne, J.; Vizvary, Z. Managing the heat: In-Vessel Components. *Philos. Trans. R. Soc. A Math. Phys. Eng. Sci.* **2024**, *382*, 20230408. [CrossRef]
7. Quadling, A.; Bowden, D.; Hardie, C.; Vasanthakumaran, A. Developing power plant materials using the life cycle lens. *Philos. Trans. R. Soc. A Math. Phys. Eng. Sci.* **2024**, *382*, 20230409. [CrossRef]
8. Taneike, M.; Fujitsuna, N.; Abe, F. Improvement of creep strength by fine distribution of TiC in 9Cr ferritic heat resistant steel. *Mater. Sci. Technol.* **2004**, *20*, 1455–1461. [CrossRef]
9. Taneike, M.; Abe, F.; Sawada, K. Creep-strengthening of steel at high temperatures using nano-sized carbonitride dispersions. *Nature* **2003**, *424*, 294–296. [CrossRef]
10. Tan, L.; Katoh, Y.; Tavassoli, A.A.F.; Henry, J.; Rieth, M.; Sakasegawa, H.; Tanigawa, H.; Huang, Q. Recent status and improvement of reduced-activation ferritic-martensitic steels for high-temperature service. *J. Nucl. Mater.* **2016**, *479*, 515–523. [CrossRef]
11. Tan, L.; Parish, C.M.; Hu, X. Microstructure and property tailoring of castable nanostructured alloys through thermomechanical treatments. *J. Nucl. Mater.* **2018**, *509*, 267–275. [CrossRef]
12. Zhou, J.; Shen, Y. Progress of MX type carbonitride reinforcement in reduced activated ferrite/martensitic heat-resistant steel. *Mater. Rep.* **2019**, *33*, 1793–1800. [CrossRef]
13. Jun, S.Y.; Kim, T.Y.; Im, S.Y.; Kim, C.W.; Lee, B.H.; Moon, J.; Lee, C.H.; Hong, H.U. Atomic scale identification of nano-sized precipitates of Ta/Ti-added RAFM steel and its superior creep strength. *Mater. Charact.* **2020**, *169*, 110596. [CrossRef]
14. Fernández, P.; Hoffmann, J.; Rieth, M.; Gómez-Herrero, A. Microstructure and precipitation behavior of advanced RAFM steels for high-temperature applications on fusion reactors. *Mater. Charact.* **2021**, *180*, 111443. [CrossRef]
15. Klueh, R.L.; Hashimoto, N.; Maziasz, P.J. New nano-particle-strengthened ferritic/martensitic steels by conventional thermo-mechanical treatment. *J. Nucl. Mater.* **2007**, *367–370*, 48–53. [CrossRef]
16. Tan, L.; Katoh, Y.; Snead, L.L. Development of castable nanostructured alloys as a new generation RAFM steels. *J. Nucl. Mater.* **2018**, *511*, 598–604. [CrossRef]
17. Mansur, L.K. Theory and experimental background on dimensional changes in irradiated alloys. *J. Nucl. Mater.* **1994**, *216*, 97–123. [CrossRef]
18. Tan, L.; Graening, T.; Hu, X.; Zhong, W.; Yang, Y.; Zinkle, S.J.; Katoh, Y. Effects of carbonitrides and carbides on microstructure and properties of castable nanostructured alloys. *J. Nucl. Mater.* **2020**, *540*, 152376. [CrossRef]
19. Pintsuk, G.; Diegele, E.; Dudarev, S.L.; Gorley, M.; Henry, J.; Reiser, J.; Rieth, M. European materials development: Results and perspective. *Fusion Eng. Des.* **2019**, *146*, 1300–1307. [CrossRef]
20. Pintsuk, G.; Aiello, G.; Dudarev, S.L.; Gorley, M.; Henry, J.; Richou, M.; Rieth, M.; Terentyev, D.; Vila, R. Materials for in-vessel components. *Fusion Eng. Des.* **2022**, *174*, 112994. [CrossRef]
21. Klueh, R.L.; Hashimoto, N.; Maziasz, P.J. Development of new nano-particle-strengthened martensitic steels. *Scr. Mater.* **2005**, *53*, 275–280. [CrossRef]
22. Klueh, R.L.; Hashimoto, N.; Buck, R.F.; Sokolov, M.A. Potential new ferritic/martensitic steel for fusion applications. *J. Nucl. Mater.* **2000**, *283–287*, 697–701. [CrossRef]
23. Hasegawa, T.; Tomita, Y.; Kohyama, A. Influence of tantalum and nitrogen contents, normalizing condition and TMCP process on the mechanical properties of low-activation 9Cr-2W-0.2V-Ta steels for fusion application. *J. Nucl. Mater.* **1998**, *258–263*, 1153–1157. [CrossRef]
24. Cristalli, C.; Pilloni, L.; Tassa, O.; Bozzetto, L.; Sorci, R.; Masotti, L. Development of innovative steels and thermo-mechanical treatments for DEMO high operating temperature blanket options. *Nucl. Mater. Energy* **2018**, *16*, 175–180. [CrossRef]
25. Hoffmann, J.; Rieth, M.; Klimenkov, M.; Baumgärtner, S. Improvement of EUROFER's mechanical properties by optimized chemical compositions and thermo-mechanical treatments. *Nucl. Mater. Energy* **2018**, *16*, 88–94. [CrossRef]
26. Tan, L.; Yang, Y.; Busby, J.T. Effects of alloying elements and thermomechanical treatment on 9Cr Reduced Activation Ferritic–Martensitic (RAFM) steels. *J. Nucl. Mater.* **2013**, *442*, S13–S17. [CrossRef]
27. Puype, A.; Malerba, L.; De Wispelaere, N.; Petrov, R.; Sietsma, J. Effect of processing on microstructural features and mechanical properties of a reduced activation ferritic/martensitic EUROFER steel grade. *J. Nucl. Mater.* **2017**, *494*, 1–9. [CrossRef]
28. Klueh, R.L. Reduced-activation steels: Future development for improved creep strength. *J. Nucl. Mater.* **2008**, *378*, 159–166. [CrossRef]
29. Gilbert, M.R.; Eade, T.; Rey, T.; Vale, R.; Bachmann, C.; Fischer, U.; Taylor, N.P. Waste implications from minor impurities in European DEMO materials. *Nucl. Fusion* **2019**, *59*, 076015. [CrossRef]

30. Pilloni, L.; Cristalli, C.; Tassa, O.; Bozzetto, L.; Zanin, E.; Bettocchi, N. Development of innovative materials and thermal treatments for DEMO water cooled blanket. *Nucl. Mater. Energy* **2019**, *19*, 79–86. [CrossRef]
31. Rieth, M.; Simondon, E.; Pintsuk, G.; Aiello, G.; Henry, J.; Terentyev, D.; Puype, A.; Cristalli, C.; Pilloni, L.; Tassa, O.; et al. Technological aspects in blanket design: Effects of micro-alloying and thermo-mechanical treatments of EUROFER97 type steels after neutron irradiation. *Fusion Eng. Des.* **2021**, *168*, 112645. [CrossRef]
32. Xia, Z.X.; Zhang, C.; Yang, Z.G. Control of precipitation behavior in reduced activation steels by intermediate heat treatment. *Mater. Sci. Eng. A* **2011**, *528*, 6764–6768. [CrossRef]
33. Xia, Z.X.; Zhang, C.; Fan, N.Q.; Zhao, Y.F.; Xue, F.; Liu, S.J. Improve creep properties of reduced activation steels by controlling precipitation behaviors. *Mater. Sci. Eng. A* **2012**, *545*, 91–96. [CrossRef]
34. Zhai, X.; Liu, S.; Zhao, Y. Effect of tantalum content on microstructure and tensile properties of CLAM steel. *Fusion Eng. Des.* **2016**, *104*, 21–27. [CrossRef]
35. Wang, C.; Cui, Q.; Huo, X.; Zhang, C.; Xu, W. Design of reduced activation ferritic/martensitic steels by multiphase optimization during the entire processing. *ISIJ Int.* **2019**, *59*, 1715–1722. [CrossRef]
36. Rieth, M.; Schirra, M.; Falkenstein, A.; Graf, P.; Heger, S.; Kempe, H.; Lindau, R.; Zimmermann, H. *EUROFER 97 Tensile, Charpy, Creep and Structural Tests*; IAEA: Karlsruhe, Germany, 2003; Available online: https://inis.iaea.org/records/qjevg-ch908 (accessed on 15 October 2025).
37. Goodall, R.; Utton, C.; Gong, P.; Hardwick, L.; Nutter, J.; Allen, D.; Lin, C.J.; Slater, C.; Barnard, P.; Challenor, I.; et al. Development of a boron-containing reduced activation Ferritic-Martensitic (B-RAFM) steel. *Ironmak. Steelmak.* **2025**, *52*, 660–671. [CrossRef]
38. Chun, Y.B.; Kang, S.H.; Lee, D.W.; Cho, S.; Jeong, Y.H.; Żywczak, A.; Rhee, C.K. Development of Zr-containing advanced reduced-activation alloy (ARAA) as structural material for fusion reactors. *Fusion Eng. Des.* **2016**, *109–111*, 629–633. [CrossRef]
39. Tanigawa, H.; Shiba, K.; Sakasegawa, H.; Hirose, T.; Jitsukawa, S. Technical issues related to the development of reduced-activation ferritic/martensitic steels as structural materials for a fusion blanket system. *Fusion Eng. Des.* **2011**, *86*, 2549–2552. [CrossRef]
40. Bailey, G.W.; Vilkhivskaya, O.V.; Gilbert, M.R. Waste expectations of fusion steels under current waste repository criteria. *Nucl. Fusion* **2021**, *61*, 036010. [CrossRef]
41. Gorley, M.J. Critical Assessment 12: Prospects for reduced activation steel for fusion plant. *Mater. Sci. Technol.* **2015**, *31*, 975–980. [CrossRef]
42. Gómez-Ferrer, B.; Dethloff, C.; Gaganidze, E.; Malerba, L.; Hatzoglou, C.; Pareige, C. Nano-hardening features in high-dose neutron irradiated Eurofer97 revealed by atom-probe tomography. *J. Nucl. Mater.* **2020**, *537*, 152228. [CrossRef]
43. Wells, P.B.; Yamamoto, T.; Miller, B.; Milot, T.; Cole, J.; Wu, Y.; Odette, G.R. Evolution of manganese-nickel-silicon-dominated phases in highly irradiated reactor pressure vessel steels. *Acta Mater.* **2014**, *80*, 205–219. [CrossRef]
44. Jenkins, B.M.; Douglas, J.O.; Almirall, N.; Riddle, N.; Bagot, P.A.J.; Hyde, J.M.; Odette, G.R.; Moody, M.P. The effect of composition variations on the response of steels subjected to high fluence neutron irradiation. *Materialia* **2020**, *11*, 100717. [CrossRef]
45. Li, L.; Messler, R.W. Segregation of phosphorus and sulfur in heat-affected zone hot cracking of type 308 stainless steel. *Weld J.* **2002**, *81*, 13638336.
46. Bhattacharya, A.; Chen, X.; Graening, T.; Geringer, J.W.; Reed, J.; Henry, J.; Pilloni, L.; Terentyev, D.; Puype, A.; Byun, T.S.; et al. Irradiation hardening and ductility loss of Eurofer97 steel variants after neutron irradiation to ITER-TBM relevant conditions. *Fusion Eng. Des.* **2021**, *173*, 112935. [CrossRef]
47. Haley, J.; Jones, S.; Mehraban, S.; Lavery, N.; Cullen, J.; Carter, M.; Moody, M.; Dawson, H.; Bowden, D. Short communication: Complete dissolution of MX-phase nanoprecipitates in fusion steels during irradiation by heavy-ions. *J. Nucl. Mater.* **2024**, *596*, 155115. [CrossRef]
48. Kohyama, A.; Hishinuma, A.; Gelles, D.S.; Klueh, R.L.; Dietz, W.; Ehrlich, K. Low-activation ferritic and martensitic steels for fusion application. *J. Nucl. Mater.* **1996**, *233–237*, 138–147. [CrossRef]
49. Dai, C.; Schade, C.; Apelian, D.; Lavernia, E.J. Processing Techniques for ODS Stainless Steels. *Metall. Mater. Trans. B Process Metall. Mater. Process. Sci.* **2018**, *49*, 3043–3055. [CrossRef]
50. Rieth, M.; Aiello, G.; Zmitko, M. Status of European reduced activation ferritic/martensitic steel EUROFER97. In *Fusion Energy Technology R and D Priorities*; Elsevier: Amsterdam, The Netherlands, 2024; pp. 27–46. [CrossRef]
51. Sakasegawa, H.; Tanigawa, H.; Kano, S.; Abe, H. Material properties of the F82H melted in an electric arc furnace. *Fusion Eng. Des.* **2015**, *98–99*, 2068–2071. [CrossRef]
52. Gilbert, M.R.; Sublet, J.-C.; Forrest, R.A. Handbook of Activation, Transmutation and Radiation Damage Properties of the Elements Simulated Using FISPACT-II and TENDL-2014, Culham Centre for Fusion Energy CCFE-R(15). 2015. Available online: https://fispact.ukaea.uk/wp-content/uploads/2016/09/CCFE-R1526.pdf (accessed on 9 December 2025).
53. Duerrschnabel, M.; Jäntsch, U.; Gaisin, R.; Rieth, M. Microstructural insights into EUROFER97 batch 3 steels. *Nucl. Mater. Energy* **2023**, *35*, 101445. [CrossRef]

54. *ASTM A335/A335M-22*; Specification for Seamless Ferritic Alloy-Steel Pipe for High-Temperature Service. ASTM International: West Conshohocken, PA, USA, 2022. [CrossRef]
55. Shim, H.J.; Kim, S.; Park, B.I.; Kim, D.H.; Johansson, V. Fabrication and characteristic of the 316L(N)-IG forged block and rolled plate for application to ITER blanket shield block. *Fusion Eng. Des.* **2020**, *156*, 111738. [CrossRef]
56. Klueh, R.L.; Cheng, E.T.; Grossbeck, M.L.; Bloom, E.E. Impurity effects on reduced-activation ferritic steels developed for fusion applications. *J. Nucl. Mater.* **2000**, *280*, 353–359. [CrossRef]
57. Butterworth, G.J.; Giancarli, L. Some radiological limitations on the compositions of low-activation materials for power reactors. *J. Nucl. Mater.* **1988**, *155–157*, 575–580. [CrossRef]
58. Ehrlich, K.; Cierjacks, S.; Kelzenberg, S.; Möslang, A. The Development of Structural Materials for Reduced Long-Term Activation. In *Effects of Radiation on Materials: 17th International Symposium*; ASTM International: West Conshohocken, PA, USA, 1996; pp. 1109–1122. [CrossRef]
59. Wang, X.; Hedberg, J.; Nie, H.Y.; Biesinger, M.C.; Odnevall, I.; Hedberg, Y.S. Location of cobalt impurities in the surface oxide of stainless steel 316L and metal release in synthetic biological fluids. *Mater. Des.* **2022**, *215*, 110524. [CrossRef]
60. Niessen, F.; Nyyssönen, T.; Gazder, A.A.; Hielscher, R. Parent grain reconstruction from partially or fully transformed microstructures in MTEX. *J. Appl. Crystallogr.* **2022**, *55*, 180–194. [CrossRef]
61. Hielscher, R.; Nyyssönen, T.; Niessen, F.; Gazder, A.A. The variant graph approach to improved parent grain reconstruction. *Materialia* **2022**, *22*, 101399. [CrossRef]
62. Klimenkov, M.; Lindau, R.; Materna-Morris, E.; Möslang, A. TEM characterization of precipitates in EUROFER 97. *Prog. Nucl. Energy* **2012**, *57*, 8–13. [CrossRef]
63. Nozawa, T.; Tanigawa, H.; Kojima, T.; Itoh, T.; Hiyoshi, N.; Ohata, M.; Kato, T.; Ando, M.; Nakajima, M.; Hirose, T.; et al. The status of the Japanese material properties handbook and the challenge to facilitate structural design criteria for DEMO in-vessel components. *Nucl. Fusion* **2021**, *61*, 116054. [CrossRef]
64. Zhang, G.J.; Zhou, Y.; Yang, J.F.; Yang, H.Y.; Wang, M.M.; Jing, K.; Xie, Z.M.; Zhang, L.C.; Liu, R.; Li, G.; et al. Effect of Si content on the microstructure and mechanical properties of 9Cr-ferritic/martensitic steels. *Nucl. Mater. Energy* **2023**, *35*, 101428. [CrossRef]
65. Von Hagen, I.; Bendick, W. Creep Resistant Ferritic Steels for Power Plants. Available online: https://niobium.tech/-/media/niobiumtech/attachments-biblioteca-tecnica/nt_creep-resistant-ferritic-steels-for-power-plants.pdf (accessed on 19 November 2025).
66. Hasegawa, Y. Grade 92 creep-strength-enhanced ferritic steel. In *Coal Power Plant Materials and Life Assessment*; Elsevier: Amsterdam, The Netherlands, 2014; pp. 52–86. [CrossRef]
67. Di Gianfrancesco, A.; Cipolla, L.; Cirilli, F.; Cumino, G.; Caminada, S. Microstructural Stability and Creep Data Assessment of Tenaris Grades 91 and 911. Available online: https://www.phase-trans.msm.cam.ac.uk/2005/LINK/147.pdf (accessed on 19 November 2025).
68. Gibson, J.S.K.-L.; Carruthers, A.; Evans, B.R.S.; Haley, J.; Kuksenko, V.; Song, K.; Hewitt, L.; Jones, S.; Mehraban, S.; Lavery, N.P.; et al. Characterisation of MX Precipitate Density and Irradiation Hardening in Advanced Reduced-Activation Ferritic-Martensitic Fusion Steels. *Materialia* **2025**, 102635, *in press*. [CrossRef]
69. Puype, A.; Bonny, G.; Malerba, L.; Petrov, R.; Sietsma, J. Design of Reduced Activation Ferritic/Martensitic Steels with Improved Creep Resistance by Thermodynamic Modelling Design of Reduced Activation Ferritic/Martensitic Steels with Improved Creep Resistance by Thermodynamic Modelling. 2018. Available online: https://papers.ssrn.com/sol3/papers.cfm?abstract_id=3275451 (accessed on 17 October 2025).
70. Zhang, L.; Harrison, W.; Yar, M.A.; Brown, S.G.R.; Lavery, N.P. The development of miniature tensile specimens with non-standard aspect and slimness ratios for rapid alloy prototyping processes. *J. Mater. Res. Technol.* **2021**, *15*, 1830–1843. [CrossRef]
71. Angella, G.; Donnini, R.; Ripamonti, D.; Bonollo, F.; Cygan, B.; Gorny, M. On Ausferrite Produced in Thin Sections: Stability Assessment through Round and Flat Tensile Specimen Testing. *Metals* **2023**, *13*, 105. [CrossRef]
72. Kassaye, F.T.; Kori, T.H.; Kozłowska, A.; Grajcar, A. Experimental Investigation and FEM Simulation of the Tensile Behavior of Hot-Rolled Quenching and Partitioning 5Mn Steel. *Materials* **2025**, *18*, 868. [CrossRef] [PubMed]